Table 1
Length, Young's modulus and stiffness of the OHC in guinea pigs and mice

Animal	Location	Cell length (μm)	Young's modulus (kPa)	Stiffness (mN/m)	Reference
Mouse	Apical turn	18.3 ± 2.2	2.1 ± 0.5	4.4 ± 1.2	This study
Guinea pig	Apical turn	81.2 ± 4.8	2.0 ± 0.81	2.0 ± 0.8	Sugawara et al. [14]
Guinea pig	Basal and second turns	34.7 ± 6.2	3.7 ± 0.96	8.7 ± 3.4	Sugawara et al. [14]

realize the frequency selectivity of mammalian hearing. Although such basic structure of the basilar membrane is conserved among mammals, the difference in the size of the basilar membrane between mice and guinea pigs has to be taken into account when the stiffness of the basilar membrane is discussed. As the longitudinal stiffness of the basilar membrane has been observed to be much smaller than the transverse stiffness in a fresh preparation [30], the basilar membrane can be represented as a series of elastic beams. Thus, when the uncoiled basilar membrane is divided at intervals of δl along the longitudinal axis of the cochlea as shown in Fig. 9, the equivalent stiffness of each beam with width w and thickness t is given by

$$K = 48EI/w^3 \tag{9}$$

where E is Young's modulus, and I is the moment of inertia of the cross-sectional area which is given by

$$I = \delta l t^3/12 \tag{10}$$

Substituting Eq. (10) into Eq. (9), the equivalent stiffness of each beam K is obtained as follows:

$$K = 4E\delta l t^3/w^3 \tag{11}$$

The reported values of the width and the thickness of the basilar membrane at the apical turn of the cochlea in mice are about 164 and 8.7 μm, respectively [20], and those in guinea pigs are about 220 and 7 μm, respectively [31]. Substituting the data of the basilar membrane width and thickness of mice and guinea pigs into Eq. (11), the equivalent stiffness of the basilar membrane per unit length, i.e., $\delta l = 1.0$ μm, in mice and that in guinea pigs is calculated to be $(6.0 \times 10^{-10})E$ and $(1.3 \times 10^{-10})E$ N/m, respectively. These results indicate that the basilar membrane at the apical turn of the cochlea in mice is about 4.6 times stiffer than that in guinea pigs if Young's modulus of the basilar membrane in mice is assumed to be the same as that in guinea pigs.

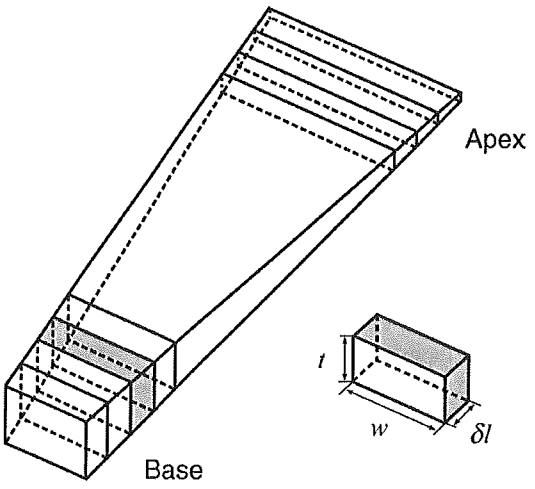

Fig. 9. Uncoiled basilar membrane represented by a series of elastic beams. The uncoiled basilar membrane is divided at intervals of δl. The width and the thickness of each beam are w and t, respectively.

The high sensitivity and sharp frequency tuning of the cochlea is realized by amplification of the basilar membrane vibration. The origin of this cochlear amplification is the force to which the basilar membrane is subjected, such force being generated by OHCs due to their electromotility. Thus, the stiffer the basilar membrane, the greater the force which must be generated by OHCs to realize the displacement of the basilar membrane vibration. In the case of mice, the basilar membrane at the apical turn of the cochlea is about 4.6 times stiffer than that of guinea pigs as mentioned above. Therefore, if the force generated by the apical turn mouse OHCs were the same as that of the apical turn guinea pig OHCs, not only the decrease of the amplitude of the basilar membrane vibration but also the lack of its tuning sharpness would result, leading to a loss of hearing sensitivity in each species. Our experimental study elucidated that the apical turn mouse OHCs are about 2.2 times stiffer than the apical turn guinea pig OHCs. According to Hooke's law, the force generated by elastic material is proportional to its stiffness for a given displacement. Based on these considerations, it can be reasonably concluded that the stiffer OHC in mice produces a greater force to amplify the vibration of the stiffer basilar membrane in the mouse cochlea.

5. Conclusions

In this study, the mechanical properties of outer hair cells (OHCs) in the apical turn of the cochlea of CBA/JNCrj strain mice were measured by atomic force microscopy. In conclusion, their Young's modulus and stiffness were 2.1 ± 0.5 kPa and 4.4 ± 1.2 mN/m, respectively. Young's modulus of the OHC in the apical turn of the cochlea in mice was roughly the same as that in the apical turn of the cochlea in guinea pigs; however, the stiffness of the former was about two times greater than that of the latter because the cell length of the former was shorter than that of the latter.

Acknowledgements

This work was supported by Grant-in-Aid for Scientific Research on Priority Areas 15086202 from the Ministry of Education, Culture, Sports, Science and Technology of Japan, by a Health and Labour Science Research Grant from the Ministry of Health, Labour and Welfare of Japan and by a grant from the Human Frontier Science Program to H.W., by Grants-in-Aid for Scientific Research 14770881 and 17591774 from the Ministry of Education, Culture, Sports, Science and Technology of Japan to N.Y. and by the Special Research Grant 11170012 from the Tohoku University 21st Century COE Program of the "Future Medical Engineering Based on Bio-nanotechnology" to M.M.

References

[1] Békésy GV. Experiments in hearing. New York, NY: McGraw-Hill Book Company, Inc.; 1960. pp. 452–455.
[2] Brownell WE, Bader CR, Bertrand D, de Ribaupierre Y. Evoked mechanical responses of isolated cochlear outer hair cells. Science 1985;227:194–6.
[3] Kachar B, Brownell WE, Altschuler R, Fex J. Electrokinetic shape changes of cochlear outer hair cells. Nature 1986;322:365–8.
[4] Ashmore JF. A fast motile response in guinea-pig outer hair cells: the cellular basis of the cochlear amplifier. J Physiol 1987;388:323–47.
[5] Santos-Sacchi J, Dilger JP. Whole cell currents and mechanical responses of isolated outer hair cells. Hear Res 1988;35:143–50.
[6] Canlon B, Brundin L, Flock A. Acoustic stimulation causes tonotopic alterations in the length of isolated outer hair cells from guinea pig hearing organ. Proc Natl Acad Sci USA 1988;85:7033–5.
[7] Zenner HP, Gitter AH, Rudert M, Ernst A. Stiffness, compliance, elasticity and force generation of outer hair cells. Acta Otolaryngol (Stockh) 1992;112:248–53.
[8] Hallworth R. Passive compliance and active force generation in the guinea pig outer hair cell. J Neurophysiol 1995;74:2319–28.
[9] Ulfendahl M, Chan E, McConnaughey WB, Prost-Domasky S, Elson EL. Axial and transverse stiffness measures of cochlear outer hair cells suggest a common mechanical basis. Pflügers Arch 1998;436:9–15.
[10] Tolomeo JA, Steele CR, Holley MC. Mechanical properties of the lateral cortex of mammalian auditory outer hair cells. Biophys J 1996;71:421–9.
[11] Oghalai JS, Patel AA, Nakagawa T, Brownell WE. Fluorescence-imaged microdeformation of the outer hair cell lateral wall. J Neurosci 1998;18:48–58.
[12] Bata TJ, Panyi G, Gásár R, Sziklai I. Active and passive behavior in the regulation of stiffness of the lateral wall in outer hair cells of the guinea-pig. Pflügers Arch 2003;447:328–36.
[13] He DZZ, Dallos P. Somatic stiffness of cochlear outer hair cells is voltage-dependent. Proc Natl Acad Sci USA 1999;96:8223–8.
[14] Sugawara M, Ishida Y, Wada H. Local mechanical properties of guinea pig outer hair cells measured by atomic force microscopy. Hear Res 2002;174:222–9.
[15] Sugawara M, Ishida Y, Wada H. Mechanical properties of sensory and supporting cells in the organ of Corti of the guinea pig cochlea—study by atomic force microscopy. Hear Res 2004;192:57–64.
[16] Zelenskaya A, Monvel JB, Pesen D, Radmacher M, Hoh JH, Ulfendahl M. Evidence for a highly elastic shell-core organization of cochlear outer hair cells by local membrane indentation. Biophys J 2005;88:2982–93.
[17] The FANTOM Consortium and the RIKEN Genome Exploration Research Group Phase I & II Team. Analysis of the mouse transcriptome based on functional annotation of 60, 770 full-length cDNAs. Nature 2002;420:563–73.
[18] Sneddon IN. The relation between load and penetration in the axisymmetric Boussinesq problem for a punch of arbitrary profile. Int J Eng Sci 1965;3:47–57.
[19] Wu HW, Kuhn T, Moy VT. Mechanical properties of L929 cells measured by atomic force microscopy: effects of anticytoskeletal drugs and membrane crosslinking. Scanning 1998;20:389–97.
[20] Keiler S, Richter CP. Cochlear dimensions obtained in hemicochleae of four different strains of mice: CBA/CaJ, 129/CD1, 129/SvEv and C57BL/6J. Hear Res 2001;162:91–104.
[21] Kalluri R, Gattone II VH, Hudson BG. Identification and localization of type IV collagen chains in the inner ear cochlea. Connect Tissue Res 1998;37:143–50.
[22] Sugawara M, Wada H. Analysis of elastic properties of outer hair cell wall using shell theory. Hear Res 2001;160:63–72.
[23] Wada H, Kimura K, Gomi T, Sugawara M, Katori Y, Kakehata S, et al. Imaging of the cortical cytoskeleton of guinea pig outer hair cells using atomic force microscopy. Hear Res 2004;187:51–62.
[24] Dimitriadis EK, Horkay F, Maresca J, Kachar B, Chadwick RS. Determination of elastic moduli of thin layers of soft material using the atomic force microscope. Biophys J 2002;82:2798–810.
[25] Holley MC, Ashmore JF. A cytoskeletal spring in cochlear outer hair cells. Nature 1988;335:635–7.
[26] Iwasa KH, Adachi M. Force generation in the outer hair cell of the cochlea. Biophys J 1997;73:546–55.
[27] Forge A. Structural features of the lateral walls in mammalian cochlear outer hair cells. Cell Tissue Res 1991;265:473–83.
[28] Raphael Y, Altschuler RA. Structure and innervation of the cochlea. Brain Res Bull 2003;60:397–422.
[29] LePage EL. Frequency-dependent self-induced bias of the basilar membrane and its potential for controlling sensitivity and tuning in the mammalian cochlea. J Acoust Soc Am 1987;82:139–54.
[30] Voldrich L. Mechanical properties of basilar membrane. Acta Otolaryngol (Stockh) 1978;86:331–5.
[31] Wada H, Sugawara M, Kobayashi T, Hozawa K, Takasaka T. Measurement of guinea pig basilar membrane using computer-aided three-dimensional reconstruction system. Hear Res 1998;120:1–6.

Phase of neural excitation relative to basilar membrane motion in the organ of Corti: Theoretical considerations

Masayoshi Andoh, Chihiro Nakajima, and Hiroshi Wada[a)]
Department of Bioengineering and Robotics, Tohoku University, 6-6-01 Aoba-yama, Sendai 980-8579, Japan

(Received 8 February 2005; revised 16 June 2005; accepted 20 June 2005)

Although the auditory transduction process is dependent on neural excitation of the auditory nerve in relation to motion of the basilar membrane (BM) in the organ of Corti (OC), specifics of this process are unclear. In this study, therefore, an attempt was made to estimate the phase of the neural excitation relative to the BM motion using a finite-element model of the OC at the basal turn of the gerbil, including the fluid-structure interaction with the lymph fluid. It was found that neural excitation occurs when the BM exhibits a maximum velocity toward the scala vestibuli at 10 Hz and shows a phase delay relative to the BM motion with increasing frequency up to 800 Hz. It then shows a phase advance until the frequency reaches 2 kHz. From 2 kHz, neural excitation again shows a phase delay with increasing frequency. From 800 Hz up to 2 kHz, the phase advances because the dominant force exerted on the hair bundle shifts from a velocity-dependent Couette flow-induced force to a displacement-dependent force induced by the pressure difference. The phase delay that occurs from 2 kHz is caused by the resonance process of the hair bundle of the IHC.
 [DOI: 10.1121/1.2000770]

PACS number(s): 43.64.Bt, 43.64.Kc [BLM] Pages: 1554–1565

I. INTRODUCTION

The mammalian cochlea consists of a fluid-filled duct that is coiled like a snail shell. Figure 1 shows a simplified sketch of the cross section of the gerbil cochlea. The cochlea is divided into three compartments, i.e., the scala vestibuli (SV), the scala media (SM), and the scala tympani (ST), by two longitudinal membranes, i.e., Reissner's membrane and the basilar membrane (BM). The vibration of the tympanic membrane and the ossicular chain, which is induced by sound, is transmitted to the BM through the cochlear fluid.

Figure 2 shows a schematic of a cross section of the organ of Corti (OC) of the gerbil. The OC, which sits on the BM, also vibrates in response to the vibration of the BM. When the OC undergoes vibration, it is conventionally thought that the hair bundles of the inner hair cell (IHC) and the outer hair cell (OHC) are deflected due to the shear motion between the tectorial membrane (TM) and the reticular lamina (RL), as shown in Fig. 2. The tip of the hair bundle of the IHC appears to be freestanding, while that of the OHC is embedded in the TM (Engströme and Engströme, 1978). The deflection of the hair bundle induces a change of the membrane potential of these cells. As shown in Fig. 2, the deflection in the direction of the tallest hair induces depolarization and that in the direction of the shortest hair induces hyperpolarization. The IHC excites the auditory nerves when its membrane potential is depolarized (Katz and Miledi, 1967) and the OHC contracts and elongates in response to the depolarization and hyperpolarization (Brownell *et al.*, 1985; Kachar *et al.*, 1986; Zenner, 1986; Ashmore, 1987; Santos-Sacchi and Dilger, 1988), respectively. This motility of the OHC generates a force (Hallworth, 1995; Iwasa and Adachi, 1997; Frank *et al.*, 1999) which amplifies the OC vibration, especially at low stimulus intensity. The auditory transduction process is therefore dependent on specific factors of the neural excitation in response to the BM vibration. Knowledge of these factors is important in the investigation of the auditory mechanics and the development of speech processors for cochlear implants.

For an investigation of the phase of the neural excitation relative to the BM motion, considerable research has been conducted. The traditional view of the response of the hair bundle of the IHC to the BM vibration is that the hair bundle of the IHC responds to the velocity of the BM vibration (Pickles, 1988) because the shear force exerted on the hair bundle is thought to be due to the shear flow between the TM and the hair bundle, the so-called Couette flow, as indicated in Fig. 2, this force being proportional to the velocity of the shear flow. As a result, if the maximum velocity of the shear flow is assumed to occur when the velocity of the BM is maximum, the maximum displacement of the tip of the hair bundle of the IHC in the direction of the tallest hair, which induces depolarization, occurs when the velocity of the BM toward the SV is maximum, i.e., when the BM crosses its equilibrium position (zero displacement) from the ST to the SV. Although the phase of the neural excitation relative to the displacement of the hair bundle is influenced by low-pass filtering at the membrane of the IHC, this influence seems to be small if the stimulus frequency is sufficiently lower than the corner frequency of the filter [approximately 200 Hz (Cheatham and Dallos, 1999)]. Therefore, according to this traditional idea, at well below 200 Hz, neural excitation would occur when the velocity of the BM toward the SV is maximum.

Ruggero and Rich (1983) measured the relationship between the neural excitation and the simultaneous BM posi-

a)Electronic mail: wada@cc.mech.tohoku.ac.jp

 0001-4966/2005/118(3)/1554/12/$22.50

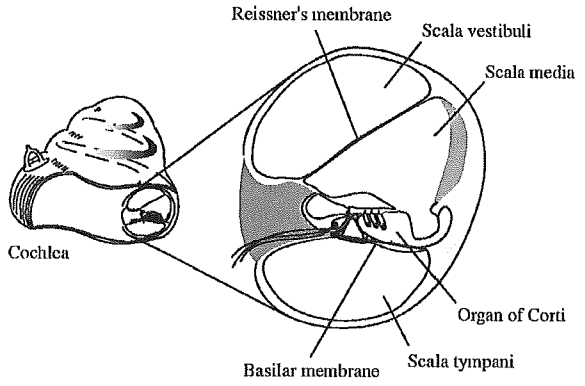

FIG. 1. Schematic of the cross section of the cochlea of the gerbil.

tion, and concluded that neural excitation occurs when the displacement of the BM toward the ST is maximum at the basal turn of the chinchilla cochlea with the characteristic frequency (CF, the most effective stimulus frequency) of 16 kHz for low-frequency stimuli (30 to 100 Hz) at 100 dB SPL. Furthermore, Wada *et al.* (2002) measured the relationship between the neural excitation and the BM motion at the

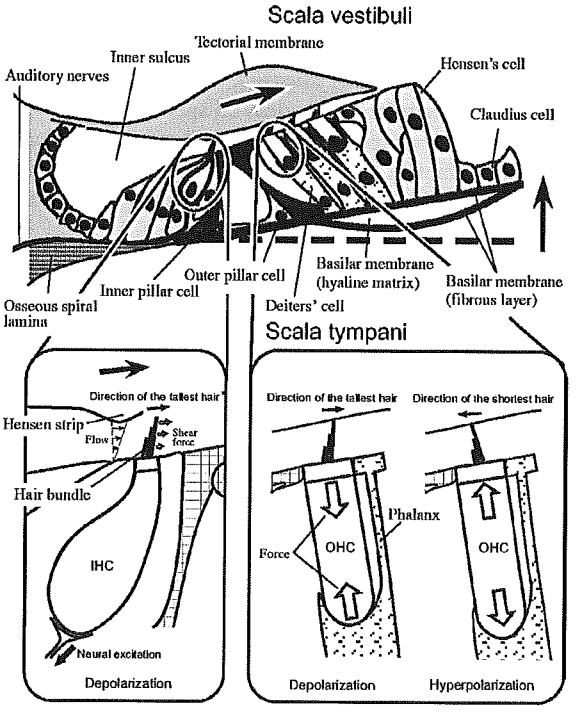

FIG. 2. Structure and mechanoelectrical transduction of the OC of the gerbil. Large arrows on the TM and beside the BM indicate the direction of their displacement. When the BM undergoes oscillatory motion, the hair bundle of the OHC is deflected by the relative displacement between the TM and the RL because its tip is embedded in the TM. On the contrary, according to the traditional idea, the hair bundle of the IHC is assumed to be vibrated by the shear force due to the shear flow between the TM and the hair bundle, and this shear force in the excitatory direction (toward the tallest hair) is thought to become maximum when the velocity of the BM toward the SV is maximum, i.e., the BM crosses its equilibrium position (zero displacement) from the ST to the SV. The deflection of the hair bundle of the IHC causes the excitation of auditory nerves, while the deflection of the hair bundle of the OHC induces the OHC motility that generates the force.

basal turn of the guinea pig cochlea with high CFs (14–22 kHz) to low-frequency stimuli (50 to 2000 Hz) at 100 dB SPL, and demonstrated that neural excitation lags behind the maximum displacement of the BM toward the SV by 20° from 50 to 100 Hz and by 45° at 500 Hz, and leads it by 45° at 2 kHz. These experimental data are therefore different from each other, as well as differing from the above-mentioned conventional idea. Thus, the phase of the neural excitation in relation to the BM motion in the cochlea has remained unclear. Cai *et al.* (2004) constructed a model of the OC by which its dynamic behavior can be analyzed. Although such a micromechanical model is expected to make it possible to investigate the phase relationship between the displacement of the hair bundle of the IHC and that of the BM in detail, they did not conduct this kind of analysis. Steele and Puria (2003) numerically analyzed the force exerted on the hair bundle of the inner hair cell by using local lubrication theory. Their research was a pioneering work, and the three rows of cilia and tip links were taken into account. However, they analyzed the vibration of the OC until 300 Hz, although the CF of their model was higher than 10 kHz. In addition, the mechanism of the force generation was not discussed.

In this study, first, a finite-element model of the OC and finite-element models of the lymph fluid surrounding the OC and of such fluid in the sub-TM space, which is a narrow space between the TM and RL, were constructed. Using these models, the phase of the displacement of the hair bundle of the IHC relative to the BM motion was then calculated. Finally, by considering the phase delay due to the low-pass filtering at the membrane of the IHC, the phase of the neural excitation relative to the BM motion was estimated.

II. MODEL OF THE ORGAN OF CORTI

A. Modification of the previous model

In a previous study (Andoh and Wada, 2004), although the geometry of the OC at the basal turn of the gerbil cochlea, where the CF is approximately 16 kHz, was reproduced based on measurement in the hemicochlea of the gerbil (Edge *et al.*, 1998; Richter *et al.*, 2000), the shapes of the TM, Deiters' cells, Hensen's cells, pillar cells, and the inner sulcus were not realistic. In addition, the homogeneous layer, the so-called hyaline matrix, between the fibrous layers in the BM, was neglected. Furthermore, as the lymph fluid in the sub-TM space was omitted, the dynamic behavior of the hair bundle of the IHC could not be analyzed. Therefore, the following additional features were incorporated in the modified model.

(a) Realistic shapes of the TM, Deiters' cells, Hensen's cells, pillar cells, and the inner sulcus.
(b) Inclusion of the hyaline matrix in the BM.
(c) Modeling of the lymph fluid in the sub-TM space.

Figure 3(a) shows the previous model of the OC, and Fig. 3(b) shows the modified model of the OC. Shapes of the TM, Deiters' cells, Hensen's cells, pillar cells, and the inner sulcus were determined based on the measurement results of

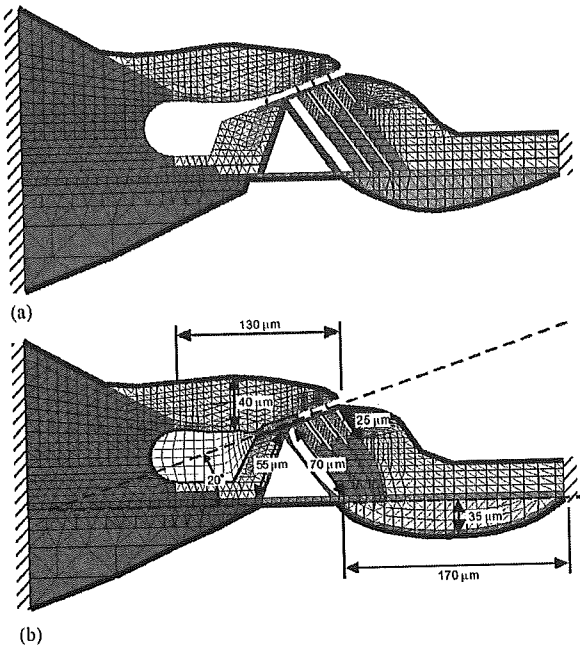

FIG. 3. Model of the OC. (a) Previous model of the OC. (b) Modified model of the OC. Each shade of gray in the model indicates a portion with the same mechanical properties. Thick lines surrounding the model indicate the fluid-structure interface of the model.

the OC in the hemicochlea of the gerbil (Richter, 2003). Although the constituents of the hyaline matrix in the BM are unknown, its structure is similar to the gel-like structure of the TM. Young's modulus of the hyaline matrix was therefore assumed to be the same as that of the TM. Table I shows all mechanical properties assigned to the models.

The boundary conditions of the models of the OC and the lymph fluid are the same as those in the previous study. They were validated by comparing the experimental data, i.e., the pressure in the ST (Olson, 2001) and the frequency characteristics of the velocity of the BM (Ren and Nuttall, 2001), with the numerical results in the previous study (Andoh and Wada, 2004). As the force generated by the OHC motility is not taken into account, the simulation is limited to the passive cochlea, i.e., OHCs are dysfunctional, or to the active cochlea, i.e., OHCs are functional when the level of the input stimulation is greater than 100 dB SPL (Ren and Nuttall, 2001).

TABLE I. Mechanical properties assigned to the models of the OC and lymph fluid. The stiffness of the hair bundle relative to the displacement of its tips is 2.5×10^{-3} N/m (Langer *et al.*, 2001). The density and viscosity of the lymph fluid are 1.0×10^{3} kg/m^3 and 1.0×10^{-3} Pa·s, respectively, which are equal to those of water.

	Young's modulus (N/m^2)	Poisson's ratio
BM (fibrous layer)	1.0×10^{7}	0.3
BM (hyaline matrix)	3.0×10^{4}	0.49
Deiters' cell	1.0×10^{7}	0.3
Hair bundle	1.0×10^{7}	0.3
Hensen's cell	5.0×10^{3}	0.49
IHC	1.0×10^{4}	0.49
Kimura's membrane	1.0×10^{6}	0.3
Osseous spiral lamina	2.0×10^{10}	0.3
OHC	1.0×10^{4}	0.49
Phalanx	1.0×10^{7}	0.3
Pillar cell	1.0×10^{9}	0.3
RL	1.0×10^{9}	0.3
TM	3.0×10^{4}	0.49

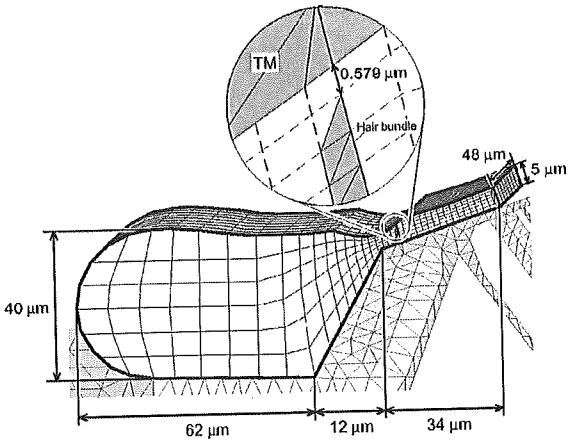

FIG. 4. Model of the lymph fluid in the sub-TM space. The sub-TM space is a fluid-filled space below the TM. It was modeled from the inner sulcus to the narrow space between the hair bundle of the IHC and that of the first row of the OHC. The height of the hair bundle of the IHC is 4.3 μm, and its shape is sharply wedged. The number of nodes is 2128 and the number of elements is 1554.

B. Lymph fluid in the sub-TM space

1. Model of the sub-TM space

To simulate the dynamic behavior of the hair bundle of the IHC, the pressure around the hair bundle must be analyzed. The model of the sub-TM space was therefore constructed as shown in Fig. 4. The width in the longitudinal direction (normal to the paper) and boundary conditions of the sub-TM model are the same as those of the SV and ST models (Andoh and Wada, 2004), i.e., the width in the longitudinal direction is 48 μm and free-flux boundary conditions are assigned to both longitudinal ends. The distribution of the velocity of the fluid around the hair bundle of the OHC was assumed to be the same as that of the hair bundle itself, due to the fact that its tip is embedded in the TM. In addition, as the hair bundle arranged in a W-shaped formation accounts for 80% of the diameter of the OHC, we assumed that the flow in the gap between the hair bundles of the OHCs in the same row was negligibly small. As a result, the sub-TM space was modeled up to the hair bundle of the first row of OHCs. These assumptions lead to the idea that the lymph fluid beyond the hair bundle of the first row of OHCs does not have an effect on the behavior of the lymph fluid around the hair bundle of the IHC. Although the tip of the hair bundle of the IHC is hemispherical, that of the model employed in this study is sharply wedged due to refinement of the mesh. The geometry of the space between the TM and the tip of the hair bundle of the IHC was determined based on a micrograph taken at the basal turn in the gerbil cochlea (Richter, 2003). The intervals of the mesh in the

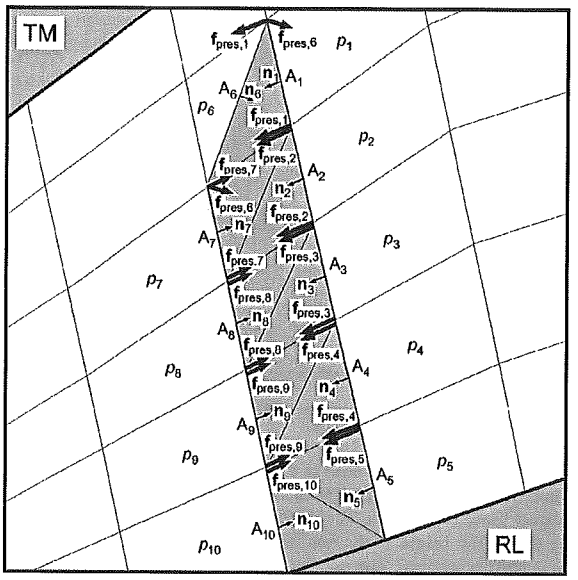

FIG. 5. Force induced by the pressure difference and exerted on the hair bundle. The pressures in the fluid elements (light gray areas) adjacent to the structural elements of the hair bundle were converted to the force vector $\mathbf{f}_{pres,n}$ at each node on the hair bundle. The force vectors at the attachment to the RL were omitted because they have no influence on the dynamic behavior of the hair bundle.

cross section are varied to avoid severe distortion of the cubic shape of the element, and result in 6×37 elements in one cross section, which make it possible to evaluate the pressure around the hair bundle of the IHC. The interval of the mesh in the longitudinal direction is 6 μm, which is the same as that in the SV and ST models.

2. Forces exerted on the hair bundle of the IHC

The pressure difference between the left and right sides of the hair bundle induces force that is exerted on the hair bundle of the IHC. In addition, as the pressure difference between the left and right sides and the relative velocity of the TM in relation to the hair bundle induce fluid flows in the narrow space, shear forces generated by these flows, i.e., Poiseuille flow and Couette flow, are considered to be exerted on the hair bundle. These three types of forces are therefore considered to be exerted on the hair bundle of the IHC.

a. Force induced by the pressure difference Figure 5 shows the force vectors induced by the pressure around the hair bundle and exerted on the hair bundle. The force vector $\mathbf{f}_{pres,n}$ on each node of the structural element of the hair bundle caused by the pressure is obtained by

$$\mathbf{f}_{pres,n} = \frac{1}{2} p_n A_n \mathbf{n}_n, \tag{1}$$

where p_n is the pressure in the fluid element adjacent to the structural element of the hair bundle, A_n is the area of contact between the fluid and structural element, and $\mathbf{n}_n$ is a unit normal vector of the fluid-structure interface. The sum of force vectors over nodes on the hair bundle is the force induced by the pressure difference between the left and right sides of the hair bundle.

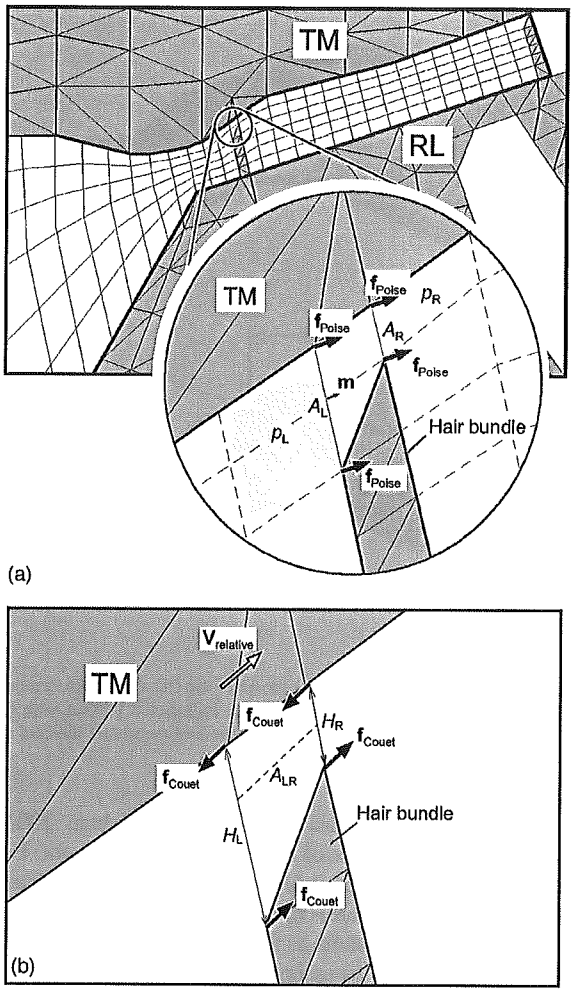

FIG. 6. Shear forces exerted on the hair bundle. (a) Force induced by Poiseuille flow. Light gray areas indicate the places where the mean pressures were calculated. Poiseuille flow occurs in the gap between the TM and the hair bundle because of the difference between the mean pressure at the left side of the gap p_L and that at the right side of the gap p_R. The force vector induced by Poiseuille flow $\mathbf{f}_{Poise}$ is in equilibrium with the difference between the product of the pressure and the cross-sectional area at the left side of the gap between the TM and the hair bundle and that at the right side of the gap. (b) Force induced by Couette flow. Couette flow in the gap between the TM and the hair bundle results from the relative velocity $V_{relative}$ of the TM in relation to the hair bundle. The force vector induced by Couette flow $\mathbf{f}_{Couet}$ is a product of the viscosity and the velocity gradient between the TM and the hair bundle.

b. Analytical deviation of the shear forces Due to computer memory size limitation, the mesh intervals in the sub-TM model are insufficiently fine for an analysis of the distribution of the fluid velocity in the gap between the TM and the RL, which is the space bounded by the TM, RL, and light gray areas shown in Fig. 6(a). Therefore, the shear forces induced by the fluid flow and exerted on the hair bundle were derived analytically.

Figure 6(a) shows Poiseuille flow-induced shear force exerted on the hair bundle and the TM. The sum of Poiseuille flow-induced shear force exerted on the hair bundle and the

TM was assumed to be the same as the difference between the product of the pressure and the cross-sectional area at the left side of the gap between the TM and the hair bundle and that at the right side. As there are two structural element nodes on each surface facing the gap between the TM and the hair bundle, the force vector $\mathbf{f}_{\text{Poise}}$ on each node of the structural element caused by Poiseuille flow is given by

$$\mathbf{f}_{\text{Poise}} = \frac{1}{4}(p_{\text{L}}A_{\text{L}} - p_{\text{R}}A_{\text{R}})\mathbf{m}, \tag{2}$$

where p_{L} and p_{R} are the mean pressures in the fluid elements adjacent to the left and right sides of the gap between the TM and the hair bundle shown by light gray areas in Fig. 6(a), A_{L} and A_{R} are the cross-sectional areas at the left and right sides of the gap, respectively, and $\mathbf{m}$ is a unit normal vector of the constant pressure line. Figure 6(b) shows Couette flow-induced shear force exerted on the hair bundle and the TM. After Arnell *et al.* (1991), the force vector $\mathbf{f}_{\text{Couet}}$ on each node of the structural element facing the gap between the TM and the hair bundle caused by Couette flow is given by

$$\mathbf{f}_{\text{Couet}} = \frac{1}{2}\mu\frac{\mathbf{V}_{\text{relative}}}{(H_{\text{L}} - H_{\text{R}})}A_{\text{LR}}\ln\frac{H_{\text{L}}}{H_{\text{R}}}, \tag{3}$$

where $\mathbf{V}_{\text{relative}}$ is the relative velocity vector of the TM in relation to the hair bundle, H_{L} and H_{R} are heights at the left and right sides of the gap between the TM and the hair bundle, respectively, A_{LR} is the area of the cross section between the left and right sides of the gap and parallel to $\mathbf{V}_{\text{relative}}$, and μ is the viscosity of the lymph fluid.

c. Numerical analysis of the shear forces To validate the analytically obtained shear forces exerted on the hair bundle represented by Eqs. (2) and (3), the shear forces were numerically analyzed by using the model of the gap between the TM and the hair bundle of the IHC, as shown in Fig. 7(a). The width in the longitudinal direction (normal to the paper) and boundary conditions of this model are the same as those of the other fluid models, i.e., the width in the longitudinal direction is 48 μm and free-flux boundary conditions are assigned to both longitudinal ends. In the case of Poiseuille flow, the pressures at the left and right sides of the gap between the TM and the hair bundle, i.e., p_{L} and p_{R}, are applied to the elements at the left and right sides of this model [light gray areas in Fig. 7(a)]. In the case of Couette flow, the relative velocity vector $\mathbf{V}_{\text{relative}}$ of the TM in relation to the hair bundle is applied as the boundary condition at the top of this model. The distribution of the velocity vector between the TM and the hair bundle is obtained according to these inputs, and the shear force vector $\mathbf{f}_{\text{shear}}$ induced by Poiseuille flow and Couette flow is then calculated as follows based on the parameters shown in Fig. 7(b):

$$\mathbf{f}_{\text{shear}} = \frac{1}{2}\mu\sum_{n=1}^{16}\frac{\mathbf{v}_n + \mathbf{v}_{n+1}}{h_n + h_{n+1}}A_{\text{top},n}, \tag{4}$$

where $\mathbf{v}_n$ is the velocity vector at nodes proximate to the hair bundle, h_n is the height of the fluid element adjacent to the hair bundle, and $A_{\text{top},n}$ is the area of contact between the fluid element and the hair bundle. By comparing this numerically obtained shear force with that given by Eqs. (2) and (3), the validity of the analytically obtained shear forces is examined.

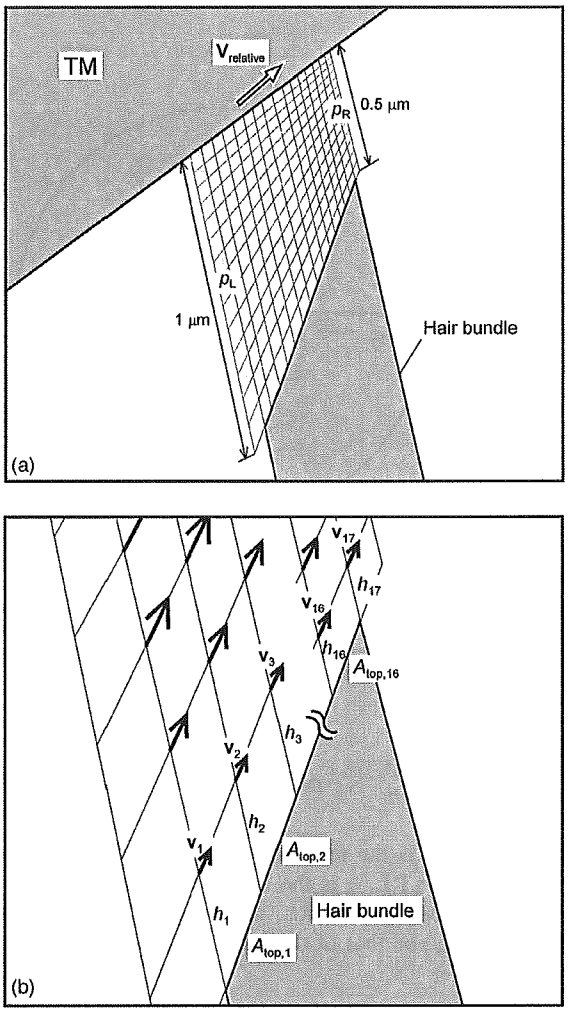

FIG. 7. Numerical analysis of the shear forces exerted on the hair bundle of the IHC. (a) Model of the gap between the TM and the hair bundle of the IHC. The number of nodes is 2040 and the number of elements is 1568. p_{L} and p_{R} are mean pressures at the left and right sides of the gap (light gray areas), respectively, and $\mathbf{V}_{\text{relative}}$ is the relative velocity of the TM in relation to the hair bundle. (b) Magnification of the model around the top of the hair bundle. Arrows indicate the velocity vectors $\mathbf{v}_n$ at nodes proximate to the hair bundle. h_n is the height of the fluid element adjacent to the hair bundle and $A_{\text{top},n}$ is the area of contact between the fluid element and the hair bundle. Based on these velocity vectors, the shear force exerted on the hair bundle is obtained from Eq. (4) for validation of the analytically obtained shear forces represented by Eqs. (2) and (3).

3. Shear force exerted on the TM and RL

In the narrow space between the TM and the RL, Couette flow is assumed to occur because of the shear motion between these two components, and the force caused by this shear motion is considered to be exerted on the TM and the RL. In this case, the force vector $\mathbf{f}_{\text{TM,RL}}$ is given by

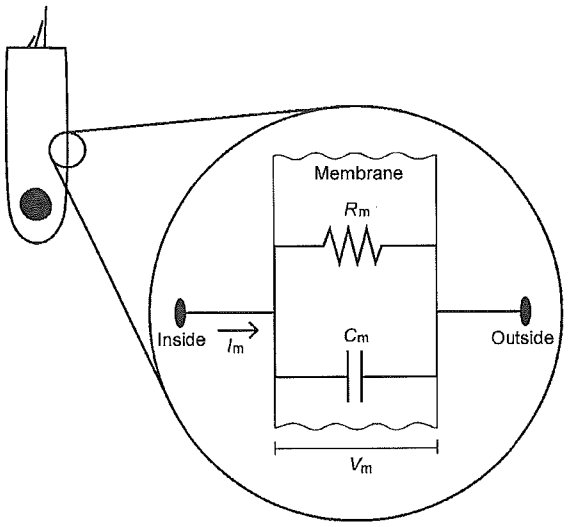

FIG. 8. Electrical circuit model of the membrane of the IHC. R_m and C_m are the membrane resistance and membrane capacitance, respectively. I_m is the current across the membrane and V_m is the membrane potential. The membrane impedance consists of a parallel connection of R_m and C_m. The membrane behaves as a low-pass filter on the membrane potential as indicated by Eq. (6).

$$\mathbf{f}_{TM,RL} = \mu \frac{\mathbf{V}_{RELATIVE}}{h} A_{TM,RL}, \tag{5}$$

where $\mathbf{V}_{RELATIVE}$ is the relative velocity vector of the TM in relation to the RL, h is the height of the narrow space between the TM and the RL, and $A_{TM,RL}$ represents the area of the TM and that of the RL facing the lymph fluid.

C. Low-pass filtering at the membrane of the IHC

Although the phase of the neural excitation relative to the BM position has not been well understood, in this study, it is assumed to be as follows: the low-pass filtering at the membrane of the IHC is effective for the entire frequency and intensity range. As shown in Fig. 8, the electrical impedance of the membrane Z_m is represented as the resistance R_m and capacitance C_m in parallel (Russell and Sellick, 1983). In this case, the magnitude $|V_m|$ and the phase θ of the membrane potential relative to the current I_m across the membrane are given by

$$|V_m| = \frac{R_m}{\sqrt{1 + \left(\frac{\omega}{\omega_0}\right)^2}} |I_m|, \tag{6}$$

$$\theta = -\arctan\left(\frac{\omega}{\omega_0}\right), \tag{7}$$

where ω is the angular frequency of the stimulus and $\omega_0 = 1/R_m C_m$ represents the corner frequency, which is assumed to be 200 Hz (Cheatham and Dallos, 1999). Equation (6) represents the behavior of the membrane as a low-pass filter of the membrane potential.

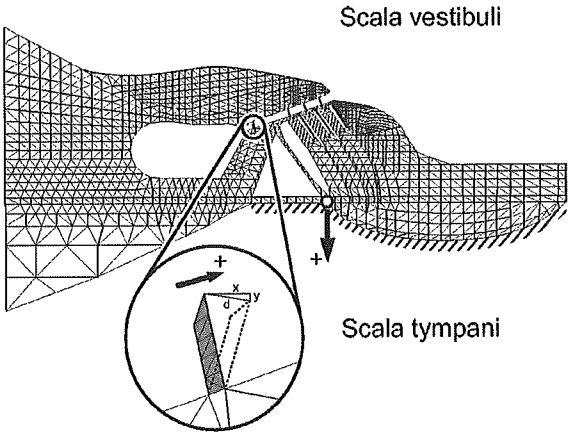

FIG. 9. A schematic of the model of the OC showing the stimulation of the model and the method of measurement. Hatching under the BM indicates the site where a sinusoidal pressure of 2 Pa is applied to the model of the OC as an initial pressure. The white circle on the BM indicates the point of displacement measurement. Positive displacement of the BM and that of the hair bundle were defined as that toward the ST and that in the excitatory direction (toward the tallest hair), respectively. A positive driving force exerted on the hair bundle was defined as that in the excitatory direction of the hair bundle.

D. Numerical procedure

Using the models mentioned above, the dynamic behavior of the OC, including the hair bundle of the IHC, was obtained from 10 Hz to 30 kHz when a sinusoidal pressure of 2 Pa was applied to the bottom of the OC, as shown in Fig. 9. The basic procedure for coupling the fluid and structure models is the same as that in the previous study (Andoh and Wada, 2004), but the forces exerted on the hair bundle of the IHC are newly taken into consideration. The revised procedure is as follows: First, the stimulus frequency is fixed to a specific frequency. As shown in Fig. 10, in time Step 1, initial pressure p^1_{INT} is applied to the model of the OC and the velocity vector of the OC $\partial \mathbf{u}^1_s / \partial t$ is obtained, where p_{INT} is the pressure initially applied to the model of the OC. Then, applying this obtained velocity vector $\partial \mathbf{u}^1_s / \partial t$ to the SV, ST, and sub-TM models as a fluid velocity vector $\mathbf{v}^0_f$ over a fluid-structure interface, the pressure p^1_{OC} in the SV, the ST and the sub-TM space caused by the movement of the OC is obtained. In time Step 2, the force vector $\mathbf{f}^1_{pres,n}$ induced by the pressure difference between the left and right sides of the hair bundle and Poiseuille flow-induced force vector $\mathbf{f}^1_{Poise}$ are given by substituting the pressure p^1_{OC} into Eqs. (1) and (2), and Couette flow-induced force vector $\mathbf{f}^1_{Couet}$ is given by Eq. (3) by calculating the relative velocity vector $\mathbf{V}^1_{relative}$ of the TM in relation to the hair bundle of the IHC. The force vector $\mathbf{f}^1_{TM,RL}$ caused by the shear motion between the TM and the RL and exerted on them is given by substituting the relative velocity vector $\mathbf{V}^1_{RELATIVE}$ of the TM in relation to the RL into Eq. (5). The previously obtained pressure p^1_{OC}, the initial pressure p^2_{INT} in time Step 2, the force vectors on the hair bundle, i.e., $\mathbf{f}^1_{pres,n}$, $\mathbf{f}^1_{Poise}$, and $\mathbf{f}^1_{Couet}$, and the force vector $\mathbf{f}^1_{TM,RL}$ exerted on the TM and the RL are applied to the model of the OC. By repeating the above procedure, the displacement of the OC, three types of forces exerted on the hair bundle and the displacement of the hair bundle at a

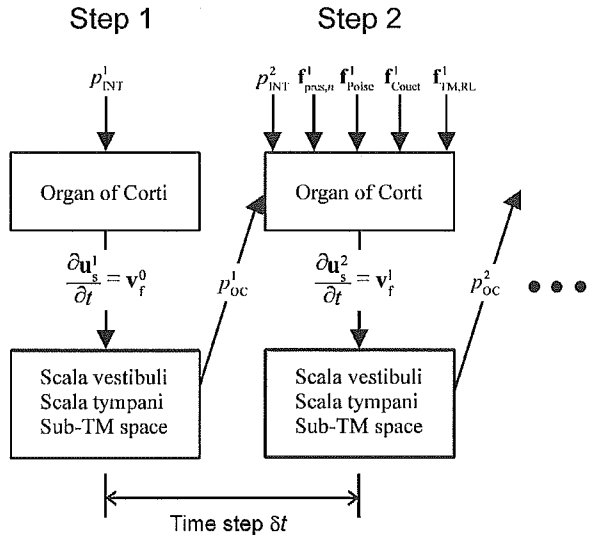

FIG. 10. Scheme of the fluid-structure interaction using the staggered approach. In time Step 1, initial pressure p^1_{INT} is applied to the model of the OC and the velocity vector of the OC $\partial \mathbf{u}^1_s/\partial t$ is obtained, where p_{INT} is an applied sinusoidal pressure of 2 Pa at the bottom of the BM, as shown in Fig. 9. Then, applying this obtained velocity vector $\partial \mathbf{u}^1_s/\partial t$ to the SV, ST, and sub-TM models as a fluid velocity vector $\mathbf{v}^0_f$ over a fluid-structure interface, the pressure p^1_{OC} in each scala, and sub-TM space caused by the movement of the OC is obtained at the same time step. In time Step 2, this obtained pressure p^1_{OC}, the initial pressure p^2_{INT} in time Step 2, the force vectors exerted on the hair bundle, i.e., the force vector $\mathbf{f}^1_{\mathrm{pres},n}$ induced by the pressure difference between the left and right sides of the hair bundle, Poiseuille flow-induced force vector $\mathbf{f}^1_{\mathrm{Poise}}$ and Couette flow-induced force vector $\mathbf{f}^1_{\mathrm{Couet}}$, and the force vector $\mathbf{f}^1_{\mathrm{TM,RL}}$ exerted on the TM and the RL are applied to the model of the OC. By repeating the above procedure, the time history of the displacement of the OC and that of the hair bundle of the IHC are obtained.

specific frequency are obtained. This analysis is conducted for stimulus frequencies from 10 Hz to 30 kHz to obtain results for this frequency range.

A numerical analysis of the shear forces exerted on the hair bundle of the IHC is also conducted for each specific frequency. The relative velocity vector $\mathbf{V}^1_{\mathrm{relative}}$ of the TM in relation to the hair bundle or the pressures at the left side p_{L} and right side p_{R} of the gap between the TM and the hair bundle are applied to the model shown in Fig. 7(a). A Navier-Stokes equation is used to analyze the dynamic behavior of the lymph fluid for these inputs, and it is solved by a Marker-and-Cell method (Harlow and Welch, 1965). The velocity vectors $\mathbf{v}^1_n$ in this space are then obtained. By substituting the obtained velocity vectors $\mathbf{v}^1_n$ into Eq. (4), the shear force $\mathbf{f}^1_{\mathrm{shear}}$ induced by Couette flow or Poiseuille flow at a specific frequency is obtained. This analysis is also conducted for stimulus frequencies from 10 Hz to 30 kHz. Consequently, the shear force for this frequency range is obtained.

III. RESULTS

A. Validation of the analytically obtained shear forces exerted on the hair bundle

Analytically obtained shear forces from Eqs. (2) and (3) are compared with those obtained numerically by using the model shown in Fig. 7(a) and from Eq. (4). Figure 11 shows

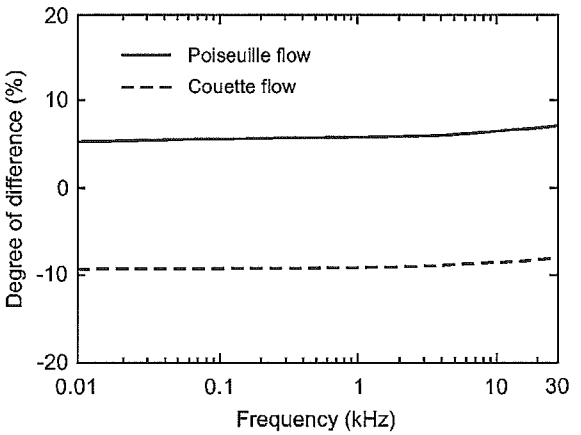

FIG. 11. Degree of difference between the analytically obtained shear forces from Eqs. (2) and (3) and those obtained numerically from Eq. (4) when a pressure of 2 Pa was applied to the bottom of the BM. The analytically obtained shear forces are in the 10% range of those obtained numerically.

the degree of difference between the analytically obtained shear forces and those obtained numerically when a pressure of 2 Pa was applied to the bottom of the BM, as shown in Fig. 9. As the degree of difference is in the 10% range for the entire frequency range, the analytically obtained results are used hereafter.

B. Driving force exerted on the hair bundle and its displacement versus BM motion

Figure 12 shows the frequency characteristics of the displacement of the BM when a pressure of 2 Pa was applied to the bottom of the BM. The displacement of the BM increases with increasing frequency toward the CF (16 kHz), and then decreases. The frequency characteristics of the magnitude of the forces exerted on the hair bundle are shown in Fig. 13. The force induced by Couette flow is larger than the other forces below 1 kHz. This relationship changes around 1 kHz, and the force induced by the pressure difference between the left and right sides of the hair bundle is larger than those induced by Poiseuille flow and Couette flow above 1 kHz.

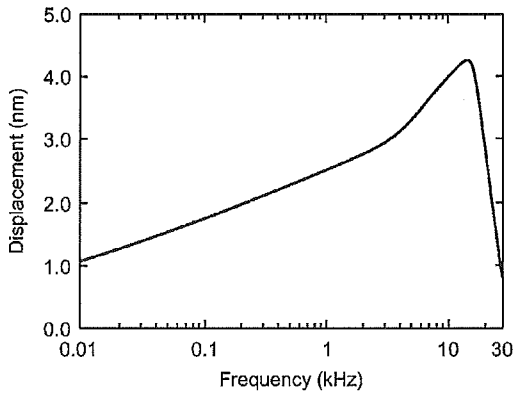

FIG. 12. Frequency characteristics of the displacement of the BM when a pressure of 2 Pa was applied to the bottom of the BM. The displacement of the BM was analyzed as the transversal displacement of the BM at the point indicated in Fig. 9 because the radial displacement of the BM was substantially small relative to the transversal one.

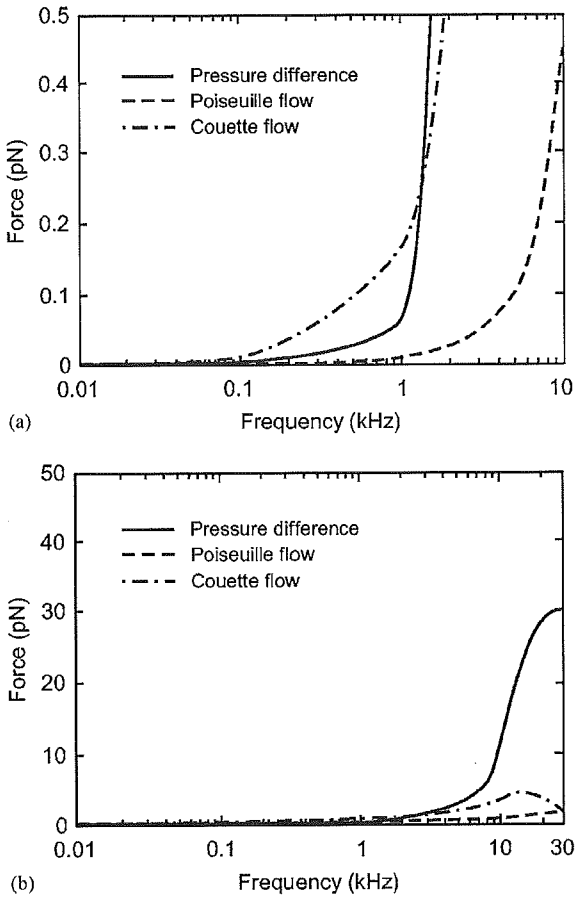

FIG. 13. Magnitudes of the three types of forces exerted on the hair bundle of the IHC versus frequency when a pressure of 2 Pa was applied to the bottom of the BM. (a) Forces plotted up to 10 kHz. (b) Forces for the entire frequency range. Below 1 kHz, the force induced by Couette flow is dominant over the forces exerted on the hair bundle. On the other hand, above 1 kHz, the force induced by the pressure difference between the left and right sides of the hair bundle is larger than the forces induced by Poiseuille flow and Couette flow.

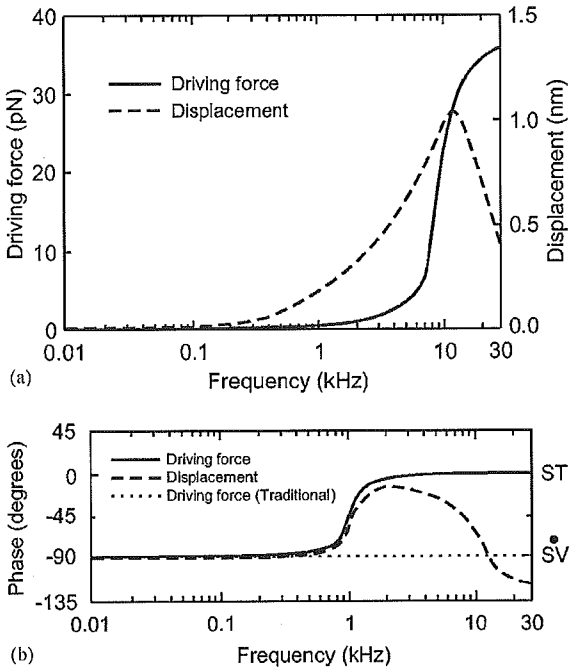

FIG. 14. Frequency characteristics of the driving force exerted on the hair bundle of the IHC and the displacement of the hair bundle when a pressure of 2 Pa was applied to the bottom of the BM. (a) The amplitude of the driving force and the displacement of the hair bundle. (b) Phases of the driving force and the displacement of the hair bundle relative to the displacement of the BM. The zero phases of the driving force and the displacement of the hair bundle relative to the displacement of the BM mean that the driving force and the displacement of the hair bundle are maximum in the excitatory direction when the BM exhibits a maximum displacement toward the ST. The increase of these phases means that their responses lag behind the BM motion. The right ordinate shows positions of the BM when the driving force or the displacement of the hair bundle is maximum in the excitatory direction. ST and SV mean positions of the BM when the BM exhibits a maximum displacement toward the ST and the BM exhibits a maximum velocity toward the SV, i.e., the BM crosses its equilibrium position (zero displacement) from the ST to the SV, respectively. As shown in Fig. 9, the displacement of the hair bundle d was analyzed based on the relative displacement of the tip of hair bundle in the radial direction x and that in the transversal direction y to those of basal end of the hair bundle on the apical surface of the IHC, i.e., $d=\sqrt{x^2+y^2}$. The phase of the driving force according to the traditional idea is plotted for reference by the dotted line.

Figure 14(a) shows the frequency characteristics of the magnitude of the driving force exerted on the hair bundle (solid line), which is a sum of the three types of forces exerted on the hair bundle, as well as those of the displacement of the hair bundle (dashed line) when a pressure of 2 Pa was applied to the bottom of the BM. The increase of the driving force is approximately proportional to the second power of the stimulus frequency. By contrast, the displacement of the hair bundle reaches a maximum at 12 kHz and then decreases. The frequency characteristics of their phases relative to the displacement of the BM are shown in Fig. 14(b). The right ordinate shows positions of the BM when the driving force or the displacement of the hair bundle is maximum in the excitatory direction. The driving force in the excitatory direction (toward the tallest hair and to the right, as indicated in Fig. 9) takes a maximum when the BM exhibits a maximum velocity toward the SV below 1 kHz. It then shows a significant phase advance relative to the BM motion around 1 kHz and takes a maximum when the BM exhibits a maximum displacement toward the ST above 1 kHz. The maximum displacement of the hair bundle in the excitatory direction occurs when the BM exhibits a maximum velocity toward the SV at 10 Hz, and according to the phase shift of the driving force, it then shows a significant phase advance relative to the BM motion up to 2 kHz, where the maximum displacement of the hair bundle in the excitatory direction lags by 13° behind the maximum displacement of the BM toward the ST. From 2 kHz, unlike the driving force, it shows a phase delay relative to the BM motion with increasing frequency, and becomes 90° at 12 kHz.

C. Neural excitation versus BM motion

Figure 15 shows the phase of the membrane potential of the IHC relative to the current across the membrane versus the stimulus frequency derived from Eq. (7). Assuming that this phase is equivalent to that of the neural excitation relative to the displacement of the hair bundle, this result implies

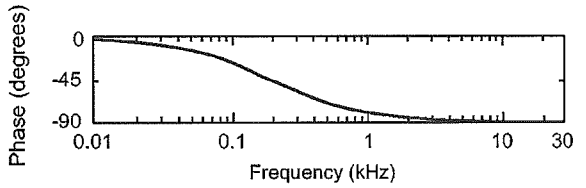

FIG. 15. Phase of the membrane potential of the IHC relative to the current across the membrane versus stimulus frequency derived from Eq. (7). The corner frequency $\omega_0 = 1/R_m C_m$ was taken to be 200 Hz.

that the neural excitation has a slight phase delay relative to the displacement of the hair bundle until 50 Hz, e.g., 3° at 10 Hz and 14° at 50 Hz. This phase delay becomes 45° at the corner frequency of 200 Hz, and then gradually approaches 90° with increasing frequency.

Figure 16 shows the frequency characteristics of the phases of the displacement of the hair bundle [dashed line: the same as the dashed line in Fig. 14(b)] and the neural excitation (solid line) relative to the displacement of the BM. The phase of the neural excitation (solid line) was obtained by adding the phase delay of the membrane potential due to the low-pass filtering at the membrane of the IHC (shown in Fig. 15) to the phase of the displacement of the hair bundle (dashed line). The right ordinate shows positions of the BM when the displacement of the hair bundle is maximum in the excitatory direction or when neural excitation occurs. Neural excitation occurs when the BM exhibits a maximum velocity toward the SV at 10 Hz. It shows a phase delay relative to

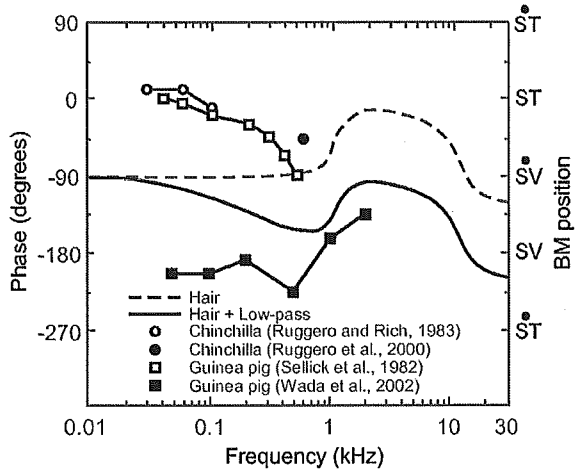

FIG. 16. Frequency characteristics of the phases of the displacement of the hair bundle (dashed line) and the neural excitation (solid line) relative to the displacement of the BM. The dashed line is the same as that in Fig. 14(b). The right ordinate shows positions of the BM when the displacement of the hair bundle is maximum in the excitatory direction or when neural excitation occurs. ST, ST, SV, and SV mean positions of the BM when the BM exhibits a maximum velocity toward the ST, the BM exhibits a maximum displacement toward the ST, the BM exhibits a maximum velocity toward the SV, and the BM exhibits a maximum displacement toward the SV, respectively. The phase of the neural excitation (solid line) was obtained by adding the phase delay of the membrane potential due to the low-pass filtering at the membrane of the IHC (shown in Fig. 15) to the phase of the displacement of the hair bundle (dashed line). Other data were taken from the literature for purposes of comparison, and sources are indicated in the legend.

the BM motion with increasing frequency up to 800 Hz and then exhibits a phase advance until the frequency reaches 2 kHz, where the neural excitation lags by 7° behind the maximum velocity of the BM toward the SV. From 2 kHz, neural excitation again shows a phase delay with increasing frequency, and at the characteristic frequency of 16 kHz, neural excitation lags by 18° behind the maximum displacement of the BM toward the SV.

IV. DISCUSSION

A. Source of the driving force exerted on the hair bundle

The traditional idea regarding the mechanism of the hair bundle oscillation in relation to the OC vibration is shown in Fig. 2. When the OC undergoes vibration, shear motion occurs between the tectorial membrane (TM) and the reticular lamina (RL). This shear motion causes Couette flow in the sub-TM space. As indicated in Eq. (3), the driving force exerted on the hair bundle due to Couette flow becomes maximum when the relative velocity of the TM in relation to the hair bundle is maximum. As a result, if the maximum relative velocity is assumed to occur when the velocity of the BM is maximum, the maximum driving force exerted on the hair bundle in the excitatory direction occurs when the velocity of the BM is maximum toward the SV at any frequency, as shown by the dotted line in Fig. 14(b). However, the solid line in Fig. 14(b) shows that the driving force in the excitatory direction becomes maximum when the BM exhibits a maximum displacement toward the ST above 1 kHz, although the numerical result in this study shows the same tendency of the driving force as that in the traditional idea below 1 kHz. This result implies that the hair bundle is driven by a different mechanism from that posited by the traditional idea.

In this study, the forces induced by the pressure difference between the left and right sides of the hair bundle and by Poiseuille flow were considered in addition to that induced by Couette flow. As shown in Fig. 13, Couette flow-induced force, which is caused by the velocity difference between the TM and the hair bundle, is larger than the other forces exerted on the hair bundle below 1 kHz. Therefore, similar to the traditional idea, the maximum driving force in the excitatory direction occurs when the velocity of the BM is maximum toward the SV below 1 kHz. By contrast, above 1 kHz, the force induced by the pressure difference is larger than the forces induced by Poiseuille flow and Couette flow. To discuss the phase of the force induced by the pressure difference relative to the BM motion, these frequency characteristics should be considered.

The pressure in an incompressible viscous fluid flow is described by the Navier-Stokes equation as follows:

$$\rho \frac{\partial \mathbf{v}}{\partial t} + \rho(\mathbf{v} \cdot \nabla)\mathbf{v} + \nabla p - \mu \Delta \mathbf{v} = 0, \tag{8}$$

where $\mathbf{v}$ is the velocity vector, p is the pressure, ρ is the density, μ is the viscosity, t is the time, and the gradient operator ∇ and the Laplacian operator Δ are defined in the following form:

$$\nabla = \left(\frac{\partial}{\partial x}, \frac{\partial}{\partial y}, \frac{\partial}{\partial z}\right), \quad \Delta = \frac{\partial^2}{\partial x^2} + \frac{\partial^2}{\partial y^2} + \frac{\partial^2}{\partial z^2}. \tag{9}$$

Equation (8) means that the pressure gradient ∇p is determined by the product of the density and the acceleration (first term), the product of the density and the velocity gradient and velocity, i.e., the momentum change (second term), and the product of the viscosity and the Laplacian of the velocity, i.e., the shear stress (fourth term). Assuming that the vibration of the OC is sinusoidal, the acceleration is 180° out of phase with the displacement. Therefore, the first term in Eq. (8) is regarded as a displacement-dependent term, and in Eq. (8), it means that the pressure is proportional to the displacement. Substituting the value of the fluid velocity (17 μm/s) around the hair bundle at 1 kHz, which was obtained from FEM analysis, into Eq. (8), the pressures in the space between the TM and the RL at 1 kHz due to the first term (displacement), the second term (momentum), and the fourth term (viscosity) were determined to be 2.2 mPa, 0.33 μPa, and 3.4 mPa, respectively. If the amplitude of the fluid velocity is assumed to be constant for any frequency, only the first term in Eq. (8) increases with increasing frequency because only this term is differentiated by time. These facts mean that, above 1 kHz, the pressure around the hair bundle is dominated by the displacement of the fluid, and the driving force is therefore synchronized with the displacement of the fluid.

Figure 17 shows the motion of the structures around the hair bundle and displacements of the fluid in the space to the right (cross-hatched area) and that to the left (hatched area) of the hair bundle. In the space to the right of the hair bundle (cross-hatched area), differences were found between the inward and outward displacements of the fluid when the BM is displaced. As the inward displacement of the fluid is defined as being positive, the sum of the inward and outward displacements of the fluid in the cross-hatched area takes maximum positive and negative values when the displacements of the BM are maximum toward the SV and the ST, respectively. The cause of the difference between the inward and outward displacements of the fluid is the volume change of the fluid above the cross-hatched area, which is indicated by the thick line in Fig. 17, due to the change of the distance between the TM and the RL. The increase of this volume results in the positive value of the sum of the inward and outward displacements of the fluid in the cross-hatched area, and *vice versa*. As mentioned in the previous paragraph, the pressure is proportional to the displacement of the fluid above 1 kHz so that the maximum positive and negative pressures in the cross-hatched area occur when the displacements of the BM are maximum toward the SV and the ST, respectively. On the other hand, in the space to the left of the hair bundle (the hatched area in Fig. 17), the pressure exerted on the hair bundle does not have a profound effect on the behavior of the hair bundle because the sum of the inward and outward displacements of the fluid is less than 14% of that in the right space (cross-hatched area) when the displacement of the BM is maximum. Consequently, above 1 kHz, the maximum driving force exerted on the hair bundle in the excitatory direction occurs when the BM exhibits a maximum displacement toward the ST. For the above-mentioned reasons, the phase relationship between the driving force and the displacement of the BM significantly changes around 1 kHz.

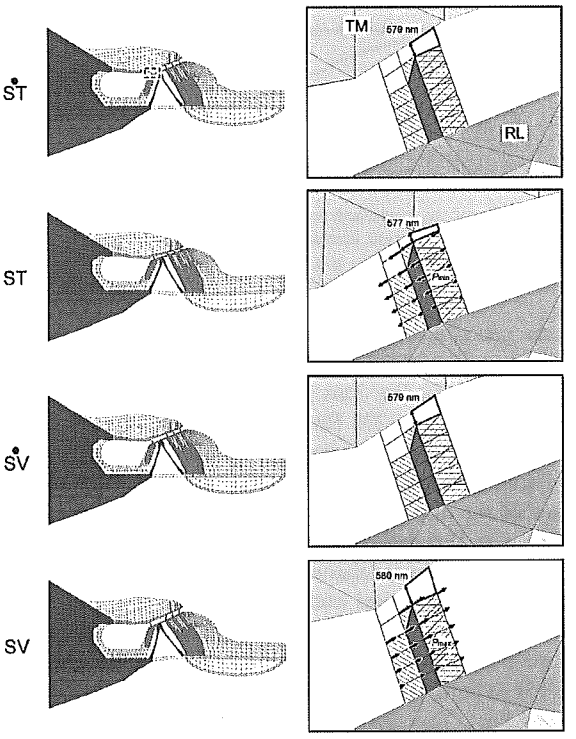

FIG. 17. Motion of the structures around the hair bundle and displacements of the fluid in the space to the right (cross-hatched area) and that to the left (hatched area) of the hair bundle when a pressure of 2 Pa was applied to the bottom of the BM at 1 kHz. ST, ST, SV, and SV indicate positions of the BM as in Fig. 16. The images on the left are the overall appearance of the model of the OC at each position of the BM and are displayed for the sake of facilitating comprehension. Those on the right are enlarged images around the hair bundle of the IHC corresponding to the dashed square in the top image on the left. Arrows indicate displacements of the fluid. However, they are not displayed when the BM exhibits maximum velocities because they are negligibly small compared with those when the BM exhibits maximum displacements. The thick line surrounding the space above the cross-hatched area is drawn on the model for clarity of its volume change caused by the change of the vertical distance between the TM and the RL, i.e., the minimum and maximum value is 577 and 580 nm, respectively. P_{max} and P_{min} mean the averaged maximum positive and negative pressures at the space to the right of the hair bundle (cross-hatched area), respectively. Displacements of the left and right images are magnified 2000 and 1000 times, respectively.

The phase of the displacement of the hair bundle is shown by the dashed line in Fig. 14(b). In a frequency range below 1 kHz, the displacement of the hair bundle follows the driving force. However, from 1 kHz, the displacement of the hair bundle gradually lags behind the driving force with increasing frequency, and its phase delay becomes 90° at 12 kHz. Assuming that the hair bundle is a simple mass-spring system and by considering the added mass of fluid to the hair bundle, the resonance frequency of the hair bundle f_{res} is analytically given by

$$f_{\text{res}} = \frac{1}{2\pi}\sqrt{\frac{k_{\text{hair}}}{m_{\text{hair}} + m_{\text{fluid}}}}, \tag{10}$$

where k_{hair} and m_{hair} are the stiffness and mass of the hair bundle, respectively, and m_{fluid} is the added mass of the fluid. k_{hair} and m_{hair} assigned to the model of the OC are 2.5×10^{-3} N/m (Langer *et al.*, 2001) and 24 pg. If the hair bundle is assumed to be a simple cylindrical structure, the added mass of the fluid is a product of the volume of the hair bundle and the density of the fluid, and so is assumed to be 20 pg. In this case, the resonance frequency of the hair bundle obtained from Eq. (10) is 12.1 kHz. Therefore, the phase delay of the displacement of the hair bundle relative to the driving force appears to occur due to the resonance process of the hair bundle. As this phase shift directly changes the timing of the depolarization of the membrane potential of the IHC, the resonance frequency of the hair bundle, as well as the phase of the driving force, is highly important when investigating the phase of the neural excitation relative to the BM motion.

Cai *et al.* (2004) constructed a model of the OC by which its dynamic behavior could be analyzed. As they assumed that the height of the gap between the TM and the RL was constant, the pressure caused by the volume change in the sub-TM space was neglected. By contrast, Hu *et al.* (1999) measured the vibration trajectories of measured points on the TM and the top of the OHCs by applying an oscillatory force via a glass paddle to the OC and reported that the direction of the vibration at the TM is approximately vertical whereas that at the top of the OHCs is horizontal. As shown in Fig. 17, the geometrical configuration of the sub-TM space, which consists of the TM, the RL, and the hair bundle of the OHC, clearly demonstrates that the distance between the TM and the tip of the hair bundle of the IHC is 579 nm when the displacement of the BM is zero and that it varies from 577 to 580 nm depending on the displacement of the BM. This causes the volume change of the sub-TM space, which must be considered when analyzing the dynamic behavior of the hair bundle of the IHC.

B. Comparison with experimental data

As the motility of the OHC was not included in the present model, and as the OC at the basal turn of the cochlea was modeled, experiments conducted at a high stimulus level and at the basal turn are appropriate for purposes of comparison. A comparison of the phase of the neural excitation relative to the BM position is presented in Fig. 16. As the data shown in the figures (Ruggero and Rich, 1983; Ruggero *et al.*, 2000; Sellick *et al.*, 1982; Wada *et al.*, 2002) had already been corrected by subtracting synaptic delay and neural travel times, i.e., 1 ms delay, from the experimental data, our numerically obtained results were compared with their data without correction. Ruggero and Rich (1983) measured the relationship between the neural excitation and the BM position at the basal turn of the chinchilla cochlea with a CF of 16 kHz to low-frequency stimuli (30 to 100 Hz) at 100 dB SPL, and concluded that the neurons from IHCs may fire in response to the displacement of the BM toward the ST. Sellick *et al.* (1982) measured the neural excitation at the basal turn of the guinea pig cochlea with CFs between 15 and 18 kHz to low-frequency stimuli (40 to 500 Hz) at 100 dB SPL, and demonstrated that the excitation of the IHC was synchronous with the maximum displacement of the BM toward the ST at 40 Hz and with the maximum velocity of the BM toward the SV at 500 Hz. Although these two experimental data show the phase delay of the neural excitation likely induced by the low-pass filtering at the membrane of the IHC as considered in the present study, they are different from our results by approximately 90°. Wada *et al.* (2002) measured the relationship between the neural excitation and the BM vibration at the basal turn of the guinea pig cochlea with high CFs (14–22 kHz) to low-frequency stimuli (50 to 2000 Hz) at 100 dB SPL and reported that neural excitation lags by 20° behind the maximum displacement of the BM toward the SV until 100 Hz and shows a phase delay relative to the BM motion with increasing frequency up to 500 Hz, where it lags by 45° behind the maximum displacement of the BM toward the SV. Neural excitation then shows a phase advance with increasing frequency and leads the maximum displacement of the BM toward the SV by 45° at 2 kHz. The phase advance with increasing frequency from 500 Hz in their data is similar to the present findings; however, the phase values are different from our results, especially at low frequencies. Although there is a hypothesis that at low frequencies the membrane potential of the IHC is modulated by the extra-cellular potential, which is the potential caused by the electrical activities of OHCs (Cheatham and Dallos, 1999), qualitative and quantitative influences of this extra-cellular potential on the membrane potential of the IHC are still unknown. A full understanding of the phase of the neural excitation relative to the BM vibration awaits further empirical investigations or refinement of our model in order to include an electrical field analysis.

V. CONCLUSIONS

In this study, first, a finite-element model of the OC and models of the lymph fluid surrounding the OC and in the sub-TM space were constructed. Using these models, the phase of the displacement of the hair bundle of the IHC relative to the BM motion was then calculated. Finally, by considering the phase delay due to the low-pass filtering at the membrane of the IHC, the phase of the neural excitation relative to the BM motion was estimated. Conclusions are as follows.

(1) Unlike the conventional idea, the phase of the driving force relative to the BM motion shows a significant phase shift around 1 kHz, i.e., although the maximum driving force in the excitatory direction occurs when the BM exhibits a maximum velocity toward the SV below 1 kHz, it also occurs when the BM exhibits a maximum displacement toward the ST above 1 kHz. This is because the dominant force exerted on the hair bundle changes from a velocity-dependent Couette flow-induced force to a displacement-dependent force induced by the pressure difference around 1 kHz.

(2) Neural excitation occurs when the BM exhibits a maximum velocity toward the SV at 10 Hz and shows a phase delay relative to the BM motion with increasing frequency up to 800 Hz. It then shows a phase advance until the frequency reaches 2 kHz, at which point the neural excitation lags by 7° behind the maximum velocity of the BM toward the SV. From 2 kHz, neural excitation again shows a phase delay with increasing frequency due to the resonance of the hair bundle, and at the characteristic frequency of 16 kHz, neural excitation lags by 18° behind the maximum displacement of the BM toward the SV.

ACKNOWLEDGMENTS

The authors wish to thank Dr. Toshiyuki Hayase for his suggestion regarding the forces induced by the fluid flow. This work was supported by a grant from the Human Frontier Science Program, by a Health and Labor Science Research Grant from the Ministry of Health, Labour, and Welfare of Japan, by Grant-in-Aid for Scientific Research (B) (2) 13557142, and Grant-in-Aid for Scientific Research on Priority Areas 15086202 from the Ministry of Education, Culture, Sports, Science and Technology of Japan, and by a 21st Century COE Program Special Research Grant of the "Future Medical Engineering Based on Bio-Nanotechnology."

Andoh, M., and Wada, H. (**2004**). "Prediction of the characteristics of two types of pressure waves in the cochlea: Theoretical considerations," J. Acoust. Soc. Am. **116**, 417–425.

Arnell, R. D., Davis, P. B., Halling, J., and Whomes, T. L. (**1991**). *Tribology: Principles and Design Applications* (Macmillan, London).

Ashmore, J. F. (**1987**). "A fast motile response in guinea-pig outer hair cells: The cellular basis of the cochlear amplifier," J. Physiol. (London) **388**, 323–347.

Brownell, W. E., Bader, D., and Ribaupierre, Y. (**1985**). "Evoked mechanical responses of isolated cochlear outer hair cells," Science **227**, 194–196.

Cai, H., Shoelson, B., and Chadwick, R. S. (**2004**). "Evidence of tectorial membrane radial motion in a propagating mode of a complex cochlear model," Proc. Natl. Acad. Sci. U.S.A. **101**, 6243–6248.

Cheatham, M. A., and Dallos, P. (**1999**). "Response phase: A view from the inner hair cell," J. Acoust. Soc. Am. **105**, 799–810.

Edge, R. M., Evans, B. N., Pearce, M., Richter, C.-P., Hu, X., and Dallos, P. (**1998**). "Morphology of the unfixed cochlea," Hear. Res. **124**, 1–16.

Engström, H., and Engström, B. (**1978**). "Structure of hairs on cochlear sensory cells," Hear. Res. **1**, 49–66.

Frank, G., Hemmert, W., and Gummer, A. W. (**1999**). "Limiting dynamics of high-frequency electromechanical transduction of outer hair cells," Proc. Natl. Acad. Sci. U.S.A. **96**, 4420–4425.

Hallworth, R. (**1995**). "Passive compliance and active force generation in the guinea pig outer hair cell," J. Neurophysiol. **74**, 2319–2329.

Harlow, F. H., and Welch, J. E., (**1965**). "Numerical calculation of time-dependent viscous incompressible flow of fluid with free surface," Phys. Fluids **8**, 2182–2189.

Hu, X., Evans, B. N., and Dallos, P. (**1999**). "Direct visualization of organ of Corti kinematics in a hemicochlea," J. Neurophysiol. **82**, 2798–2807.

Iwasa, K. H., and Adachi, M. (**1997**). "Force generation in the outer hair cell of the cochlea," Biophys. J. **73**, 546–555.

Kachar, B., Brownell, W. E., Altschuler, R., and Fex, J. (**1986**). "Electrokinetic shape changes of cochlear outer hair cells," Nature (London) **322**, 365–368.

Katz, B., and Miledi, R. (**1967**). "A study of synaptic transmission in the absence of nerve impulses," J. Physiol. (London) **192**, 407–436.

Langer, M. G., Fink, S., Koitschev A., Rexhausen, U., Hober, J. K. H., and Ruppersberg, J. P. (**2001**). "Lateral mechanical coupling of stereocilia in cochlear hair bundles," Biophys. J. **80**, 2608–2621.

Olson, E. S. (**2001**). "Intracochlear pressure measurements related to cochlear tuning," J. Acoust. Soc. Am. **110**, 349–367.

Pickles, J. O. (**1988**). *An Introduction to the Physiology of Hearing*, 2nd ed. (Academic Press, London).

Ren, T., and Nuttall, A. L. (**2001**). "Basilar membrane vibration in the basal turn of the sensitive gerbil cochlea," Hear. Res. **151**, 48–60.

Richter, C.-P. (**2003**) (private communication).

Richter, C.-P., Edge, R. M., He, D. Z. Z., and Dallos, P. (**2000**). "Development of the gerbil inner ear observed in the hemicochlea," J. Assoc. Res. Otolaryngol. **1**, 195–210.

Ruggero, M. A., Narayan, S. S., Temchin, A. N., and Recio, A. (**2000**). "Mechanical bases of frequency tuning and neural excitation at the base of the cochlea: Comparison of basilar-membrane vibrations and auditory-nerve-fiber responses in chinchilla," Proc. Natl. Acad. Sci. U.S.A. **97**, 11744–11750.

Ruggero, M. A., and Rich, N. C. (**1983**). "Chinchilla auditory-nerve response to low-frequency tones," J. Acoust. Soc. Am. **73**, 2096–2108.

Russell, I. J., and Sellick P. M. (**1983**). "Low-frequency characteristics of intracellularly recorded receptor potentials in guinea-pig cochlear hair cells," J. Physiol. (London) **338**, 179–206.

Santos-Sacchi, J., and Dilger, J. P. (**1988**). "Whole cell currents and mechanical responses of isolated outer hair cells," Hear. Res. **35**, 143–150.

Sellick, P. M., Patuzzi, R., and Johnstone, B. M. (**1982**). "Modulation of responses of spiral ganglion cells in the guinea pig cochlea by low frequency sounds," Hear. Res. **7**, 199–221.

Steele, C. R., and Puria, S. (**2003**). "Analysis of forces on inner hair cell cilia," *Biophysics of the Cochlea: From Molecule to Model* (World Scientific, Singapore), pp. 359–365.

Wada, H., Takeda, A., and Kawase, T. (**2002**). "Timing of neural excitation in relation to basilar membrane motion in the basal region of the guinea pig cochlea during the presentation of low-frequency acoustic stimulation," Hear. Res. **165**, 165–176.

Zenner, H. P. (**1986**). "Motile responses in outer hair cells," Hear. Res. **22**, 83–90.

Available online at www.sciencedirect.com
SCIENCE DIRECT®
Hearing Research 205 (2005) 262–270
HEARING RESEARCH
www.elsevier.com/locate/heares

Construction of an expression system for the motor protein prestin in Chinese hamster ovary cells

Koji Iida [a], Kouhei Tsumoto [b], Katsuhisa Ikeda [c], Izumi Kumagai [b], Toshimitsu Kobayashi [d], Hiroshi Wada [a,*]

[a] *Department of Bioengineering and Robotics, Tohoku University, 6-6-01 Aoba-yama, Sendai 980-8579, Japan*
[b] *Department of Biomolecular Engineering, Tohoku University, 6-6-07 Aoba-yama, Sendai 980-8579, Japan*
[c] *Department of Otorhinolaryngology, Juntendo University School of Medicine, 2-1-1 Hongo, Bunkyo-ku, Tokyo 113-8421, Japan*
[d] *Department of Otolaryngology – Head and Neck Surgery, Tohoku University School of Medicine, 1-1 Seiryo-machi, Sendai 980-8575, Japan*

Received 23 August 2004; accepted 15 March 2005
Available online 28 April 2005

Abstract

The electromotility of outer hair cells (OHCs) is believed to be a major factor in cochlear amplification that enables the high sensitivity of hearing in mammals. This motility is thought to be based on voltage-dependent conformational changes of a motor protein embedded in the lateral wall of the OHC. In 2000, this motor protein was identified and termed prestin. To obtain knowledge on the function of prestin, research at the molecular level is necessary. For this purpose, a method of obtaining a large amount of prestin is required. In this study, an attempt was therefore made to construct an expression system for prestin. Prestin cDNA was introduced into *Escherichia coli* (*E. coli*), insect cells and Chinese hamster ovary (CHO) cells, and the expression of prestin was examined by Western blotting. As CHO cells expressed prestin well, we generated prestin-expressing cell lines using CHO cells by limiting dilution cloning. The stable expression and the activity of prestin in generated cell lines were then confirmed. Finally, to obtain prestin from these cell lines efficiently, culture conditions of the cells were examined, and it was clarified that cells should be cultured in serum-free medium and harvested around 48 h after passage.

Keywords: Outer hair cell; Prestin; Chinese hamster ovary cell; Cloning; Stable expression

1. Introduction

Mammalian hearing sensitivity relies on a mechanical amplification mechanism based on the electromotility of outer hair cells (OHCs) (Brownell et al., 1985; Kachar et al., 1986; Zenner, 1986; Ashmore, 1987; Santos-Sacchi and Dilger, 1988). This mechanism enables the high sensitivity, wide dynamic range and sharp frequency selectivity of hearing in mammals (Dallos, 1992). The molecular basis of this mechanism is thought to be voltage-dependent conformational changes of motor proteins, which are embedded in the plasma membrane of the OHC lateral wall (Forge, 1991; Huang and Santos-Sacchi, 1993).

In 2000, Zheng et al. identified the motor protein in the gerbil cochlea and termed it prestin. Since its identification, prestin has been intensively researched to elucidate the characteristic behavior of the OHCs. As a result, it has been confirmed that prestin-transfected mammalian cells show characteristic features of the

Abbreviations: OHC, outer hair cell; *E. coli*, *Escherichia coli*; CHO, Chinese hamster ovary; MBP, maltose-binding protein; GFP, green fluorescent protein

* Corresponding author. Tel.: +81 22 795 6938; fax: +81 22 795 6939.
E-mail address: wada@cc.mech.tohoku.ac.jp (H. Wada).

0378-5955/$ - see front matter © 2005 Elsevier B.V. All rights reserved.
doi:10.1016/j.heares.2005.03.027

OHC based on its motor protein, i.e., they exhibit voltage-dependent nonlinear capacitance (Zheng et al., 2000; Ludwig et al., 2001; Santos-Sacchi et al., 2001), electromotility (Zheng et al., 2000) and force generation (Ludwig et al., 2001). It has also been clarified that both the amino and carboxyl termini are located on the intracellular side (Zheng et al., 2001) and that intracellular anions act as voltage sensors of prestin (Oliver et al., 2001). In addition, Liberman et al. (2002) generated prestin knockout mice and showed that targeted deletion of prestin in mice resulted in a loss of OHC electromotility in vitro. Such deletion has also been found to result in a 40–60 dB loss of cochlear sensitivity in vivo (Wu et al., 2004).

However, the motor function of prestin still needs to be understood at the molecular level. For this purpose, a method of obtaining a large amount of prestin as material for such research is required. In this study, an attempt was therefore made to construct an expression system for prestin. Prestin cDNA was introduced into *Escherichia coli* (*E. coli*), insect cells and Chinese hamster ovary (CHO) cells, and the expression of prestin was examined by Western blotting. As CHO cells expressed prestin, stable prestin-expressing cell lines were generated using transfected CHO cells by limiting dilution cloning. The expression of prestin and the activity of prestin in the generated cell lines were then examined by immunofluorescence experiments and patch–clamp measurements, respectively. Finally, to obtain prestin from these cell lines efficiently, the optimal culture condition of the cells was considered.

2. Materials and methods

2.1. Verification of expression in cells

Escherichia coli expression vectors pET28b (Novagen, Madison, WI), pET20b (Novagen) and pMAL-c2 (New England Biolabs, Beverly, MA) were used for the *E. coli* expression system. Gerbil prestin cDNA was inserted into these vectors. The open reading frame of the prestin cDNA was fused in a frame with the His_6-tag coding sequence of the expression vector pET28b or pET20b. For this purpose, the stop codon was removed. To express prestin as a maltose-binding protein (MBP)-fusion protein, prestin cDNA was inserted into the pMAL-c2 expression vector. The *E. coli* strains BL21 and JM109 were transformed by heat shock with pET28b or pET20b and pMAL-c2 *E. coli* expression vectors containing prestin cDNA, respectively. *E. coli* transformed with pET28b or pET20b was cultured in 200 ml 2× YT medium at 28 °C, and *E. coli* transformed with pMAL-c2 was cultured in 200 ml LB medium at 37 °C. When the bacteria had grown to an optical density at 600 nm of 0.6, IPTG was added to a final concentration of 1 mM. After 2–5 h, cells were harvested and the expression of prestin in bacteria was examined by Western blotting. When pET28b or pET20b was used, the expression was examined with anti-His_6 antibody (Invitrogen, Rockville, MD), and when pMAL-c2 was used, the expression was examined with anti-MBP antibody (New England Biolabs).

To use the baculovirus expression system, the pVL1392 transfer vector (PharMingen, San Diego, CA) was employed. Prestin cDNA fused at its 3′ end to the His_6-tag coding sequence was introduced into the pVL1392 transfer vector. Linearized baculovirus DNA (BaculoGold, Pharmingen) and the constructed pVL1392 transfer vector containing the prestin cDNA were co-transfected into Sf9 insect cells using Lipofectin Reagent (Invitrogen). The recombinant baculovirus was then amplified. Sf9 cells plated onto a 35-mm plate with 2 ml of fresh medium were infected with amplified baculovirus. After incubation for 3 days, cells were harvested and the expression of prestin in Sf9 cells was examined by Western blotting with anti-His_6 antibody.

For the mammalian expression system, the pIRES-hrGFP-1a (Stratagene, La Jolla, CA) mammalian expression vector was used. The open reading frame of the prestin cDNA was fused in the frame with the FLAG-tag of the expression vector. CHO-K1 cells (provided by the Cell Resource Center for Biomedical Research, Tohoku University) were transfected with the constructed expression vector using LipofectAMINE 2000 Reagent (Invitrogen). Transfected CHO cells were cultured in RPMI-1640 medium with 10% fetal bovine serum, 100 U penicillin/ml and 100 μg streptomycin/ml at 37 °C with 5% CO_2 for 2 days, and the expression of prestin in CHO cells was then examined by Western blotting with anti-FLAG antibody (Sigma–Aldrich, St. Louis, MO).

When Western blotting was performed, cell proteins were separated on 10% SDS–polyacrylamide gel and electroblotted onto nitrocellulose membrane. After blocking with skimmed milk, membranes were incubated with the primary antibody described above. Bands were visualized using horseradish peroxidase-conjugated secondary antibody and the ECL Western blotting detection system (Amersham–Pharmacia Biotech, Buckinghamshire, UK).

2.2. Cloning of prestin-expressing CHO cells

As prestin was expressed in CHO cells, an attempt was made to generate stable prestin-expressing cell lines using CHO cells. Wild-type prestin cDNA or C-terminal FLAG-tagged prestin cDNA contained in the pIRES-hrGFP-1a mammalian expression vectors was transfected into CHO cells using LipofectAMIN 2000 Reagent. After transfection, cells were plated out at a density of one cell/well in 96-well tissue culture plates. Plates were

incubated at 37 °C with 5% CO_2. Single colonies contained in 96-well plates were scaled up. Clones with slow growth were discarded. As the pIRES-hrGFP-1a vector includes the green fluorescent protein (GFP) gene, transfected clones were chosen based on the fluorescence of GFP using a fluorescent microscope.

2.3. Immunofluorescence experiments

To confirm the expression of FLAG-tagged prestin in the generated cell lines, immunofluorescence experiments were performed. CHO cells transfected with FLAG-tagged prestin and untransfected CHO cells were fixed with 4% formaldehyde in phosphate buffer for 5 min at room temperature and washed with PBS. The samples were then incubated with skim milk and fetal bovine serum for 30 min at 37 °C. After PBS washing, cells were incubated with anti-FLAG primary antibody in PBS with 0.1% saponin solution for 1 h at 37 °C. The samples were then washed with PBS and incubated with TRITC-conjugated anti-mouse IgG secondary antibody (Sigma–Aldrich) in PBS containing 0.1% saponin solution for 30 min at 37 °C. Finally, the samples were washed with PBS, and immunofluorescence images of the samples were obtained using a confocal laser scanning microscope (LSM-GB200, Olympus, Tokyo, Japan).

2.4. Functional analysis of the generated cell lines

To confirm the activity of prestin expressed in the generated cell lines, the electrophysiological properties of these cell lines were measured. Patch pipettes for whole-cell patch–clamp recordings were pulled from glass capillaries with a puller (PP-830, Narishige). Patch pipettes had a resistance of 2–3 MΩ when filled with an internal solution composed of 140 mM KCl, 3.5 mM $MgCl_2$, 5 mM EGTA, 5 mM Hepes, 0.1 mM $CaCl_2$ and 2.5 mM Na_2ATP, adjusted to pH 7.3. The bath solution contained 145 mM NaCl, 5.8 mM KCl, 1.3 mM $CaCl_2$, 0.9 mM $MgCl_2$, 10 mM Hepes, 0.7 mM Na_2HPO_4 and 5.6 mM glucose, adjusted to pH 7.3.

The measurement system consisted of a patch amplifier (Axopatch 200B, Axon Instruments, Foster City, CA), an A/DD/A converter (Digidata 1320A, Axon Instruments), a personal computer and a function generator (WF1944, NF Electronic Instruments, Kanagawa, Japan). Measurements of cell capacitance were performed using the membrane test feature of pCLAMP 8.0 acquisition software (Axon Instruments). A test square wave (amplitude, 20 mV; period $T = 4$ ms, i.e., frequency, 250 Hz) was generated by the personal computer controlled by pCLAMP 8.0 software and applied to the cell through the amplifier. The transient current, which is caused by the test square wave, was then sampled through the amplifier. Transient current Q, current decay τ and total resistance R_t were continuously calculated by pCLAMP 8.0 software at a resolution of 25 Hz, by averaging the responses to 10 positive and 10 negative consecutive test steps, and measured values of these parameters were stored in the computer. Access resistance R_a, membrane resistance R_m and membrane capacitance C_m were then obtained by substituting Q, τ and R_t into the following equations (Huang and Santos-Sacchi, 1993):

$$R_a = \frac{R_t \tau V_c}{Q R_t + \tau V_c}, \tag{1}$$

$$R_m = R_t - R_a, \tag{2}$$

$$C_m = \left(\frac{R_t}{R_m}\right)^2 \frac{Q}{V_c}, \tag{3}$$

where V_c is a voltage step. To determine the voltage dependence of membrane capacitance, triangular voltage ramps were superimposed on the above-mentioned square test wave. This triangular voltage wave (period $T = 2$ s) was generated by the function generator and swung the cell potential from −140 to +70 mV (Frolenkov et al., 2000).

After the measurements, the membrane capacitance was plotted versus the membrane potential. The membrane capacitance was fitted to the derivative of a Boltzmann function (Santos-Sacchi, 1991)

$$C_m(V) = C_{lin} + \frac{Q_{max}}{\alpha e^{\frac{V-V_{1/2}}{\alpha}}\left(1 + e^{-\frac{V-V_{1/2}}{\alpha}}\right)^2}, \tag{4}$$

where C_{lin} is the linear capacitance, Q_{max} is the maximum charge transfer, V is the membrane potential and $V_{1/2}$ is the voltage at half-maximal charge transfer. In Eq. (4), α is the slope factor of the voltage dependence of the charge transfer and is given by

$$\alpha = kT/ze, \tag{5}$$

where k is Boltzmann's constant, T is absolute temperature, z is valence and e is electron charge. When the membrane capacitance of the cell was fitted to Eq. (4) with the correlation coefficient $R \geqslant 0.98$, the cell was defined as showing nonlinear capacitance.

2.5. Outer hair cell isolation

To compare the properties of prestin expressed in generated cell lines with those in OHCs, membrane capacitance of OHCs from guinea pigs was measured in advance. Guinea pigs weighing between 200 and 500 g were used. They were decapitated and temporal bones were removed. After the bulla had been opened, the cochlea was detached and transferred to an experimental bath. The bony shell covering the cochlea was removed and the organ of Corti was gently dissociated from the basilar membrane. The OHCs were isolated

by gently pipetting the organ of Corti after enzymatic incubation with dispase (500 U/ml). The care and use of the animals in this study were approved by the Institutional Animal Care and Use Committee of Tohoku University, Sendai, Japan.

2.6. Suspension culture of FLAG-tagged prestin-expressing CHO cells

Generally, a large number of cells can be obtained efficiently and conveniently by suspension culture (Avgerinos et al., 1990). Accordingly, FLAG-tagged prestin-expressing CHO cells, which are essentially adhesive cells, were adapted from serum supplemented medium to CHO-S-SFM II (Invitrogen) serum-free medium. They were then statically subcultured in this medium because it enables CHO cells to grow in suspension. To examine the activities of prestin, which were expressed in the cells cultured in the CHO-S-SFM II medium, the electrophysiological properties of the cells were measured using patch–clamp recordings.

To obtain prestin from the cells efficiently, the time course of the quantity of the cells and the amount of prestin per unit number of cells, i.e., expression level, were examined to consider when cells should be harvested. The quantity of the cells was evaluated by cell density, i.e., counting cell number per unit volume of culture medium with a hemocytometer every 12 h after passage. To examine the expression level of prestin, first, aliquots of 5×10^4 cells were harvested every 12 h and Western blotted with anti-FLAG primary antibody and anti-mouse IgG horseradish peroxidase-conjugated secondary antibody (New England Biolabs) after electrophoresis on a 10% SDS–polyacrylamide gel. Proteins were then visualized using the ECL Western blotting detection system and a luminescent image analyzer (LAS-1000, Fuji Film, Tokyo, Japan), and the luminescence intensity of the bands, which indicate FLAG-tagged prestin, was measured.

3. Results

3.1. Prestin expression in cells

Prestin cDNA was introduced into *E. coli*, Sf9 insect cells and CHO cells, and the expression of prestin was examined by Western blotting. Prestin has a predicted molecular weight of 81.4 kDa. The results of Western blotting used to assay the expression of prestin are shown in Fig. 1. When the *E. coli* expression system was employed, bands, which show the expression of prestin, were not detected, although three kinds of expression vectors were used for transformation. By contrast, when the baculovirus expression system was used, a band around 65 kDa and some weak bands below that were detected in transfected cells, but no band

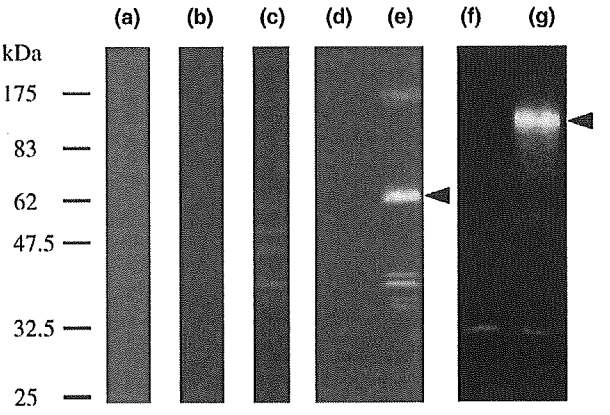

Fig. 1. Expression of prestin examined by Western blot analysis. (a) *E. coli* BL21 transformed with the pET28b vector containing prestin cDNA. (b) *E. coli* BL21 transformed with the pET20b vector containing prestin cDNA. (c) *E. coli* JM109 transformed with the pMAL-c2 vector containing prestin cDNA. (d) Untransfected Sf9 insect cells. (e) Sf9 insect cells transfected with the pVL1392 vector containing prestin cDNA. (f) Untransfected CHO cells. (g) CHO cells transfected with the pIRES-hrGFP-1a vector containing prestin cDNA. Arrows indicate the prestin bands. Bands were not detected using the *E. coli* expression system. By contrast, bands showing prestin were detected when a baculovirus expression system or a mammalian expression system was used.

was detected in untransfected cells. When the CHO cell expression system was used, a strong, broad band around 90 kDa was detected in transfected cells, and bands around 30 kDa were detected in both untransfected cells and transfected cells. These results indicate that the prestin is expressed well in CHO cells. An attempt was therefore made to construct stable prestin-expressing cell lines using transfected CHO cells.

3.2. Generation of prestin-expressing CHO cell lines

Cells were plated out into 96 wells after transfection. In the case of CHO cells transfected with wild-type prestin, 26 wells contained a single colony, the growth of 22 of them being good. In two of their clones, it was confirmed by fluorescence observation that all cells expressed GFP. In the case of CHO cells transfected with FLAG-tagged prestin, 21 wells contained a single colony, the growth of 13 of them being good. In two of their clones, it was confirmed by fluorescence observation that all cells expressed GFP. These four clones were then passaged over 40 times for 4 months, examination revealing that they retained the expression of the GFP. One of the obtained wild-type prestin-expressing cell lines and one of the FLAG-tagged prestin-expressing cell lines were then used for the following analysis.

3.3. Expression of prestin in generated cell lines

Although introduction of the expression vector and GFP expression were clarified by fluorescence

observation, the expression of prestin had not yet been elucidated. The expression of FLAG-tagged prestin in generated cells, which were subcultured for 4 months, was therefore examined by immunofluorescence experiments. Results are shown in Fig. 2. The plasma membrane of 83% of the generated cells was stained. By contrast, untransfected cells were not stained.

3.4. Activity of prestin expressed in generated cell lines

After the expression of prestin was confirmed by immunofluorescence staining, the activity of prestin expressed in the generated cell lines was examined by patch–clamp measurements. Before obtaining the electrophysiological properties of CHO cells, those of OHCs of guinea pig were measured. They exhibited bell-shaped nonlinear membrane capacitance in response to ramping of the transmembrane voltage (Fig. 3). This nonlinear membrane capacitance was well fitted to a derivative of a Boltzmann function (Eq. (4)). In a group of 11 cells, the fitting parameters of Eq. (4) were obtained as C_{lin} = 26.8 ± 3.7 pF, Q_{max} = 2.88 ± 0.65 pC, α = 28.4 ± 2.3 mV and $V_{1/2}$ = −40.1 ± 9.5 mV (mean ± SD) (Table 1).

The electrophysiological properties of wild-type prestin-expressing CHO cells and those of FLAG-tagged prestin-expressing CHO cells were then measured. The membrane capacitance versus membrane potential measured in a wild-type prestin-expressing CHO cell and that measured in a FLAG-tagged prestin-expressing CHO cell are shown in Fig. 4(a) and (b), respectively. As shown in these figures, wild-type prestin-expressing cells and FLAG-tagged prestin-expressing cells exhibited bell-shaped nonlinear membrane capacitance fitted to Eq. (4). In the case of wild-type prestin-expressing cells, 20 of 57 randomly measured cells showed nonlinear membrane capacitance, the fitting parameters of Eq. (4) being obtained as C_{lin} = 19.7 ± 4.1 pF, Q_{max} = 75.5 ± 37.3 fC, α = 38.1 ± 4.8 mV and $V_{1/2}$ = −74.8 ± 11.6 mV (mean ± SD) (Table 1). In the case of FLAG-tagged prestin-expressing cells, 19 of 53 randomly measured cells showed nonlinear membrane capacitance, the fitting parameters of Eq. (4) being obtained as C_{lin} = 24.5 ± 8.3 pF, Q_{max} = 101.3 ± 51.9 fC, α = 38.0 ± 5.5 mV and $V_{1/2}$ = −73.0 ± 12.9 mV (mean ± SD) (Table 1). By contrast, untransfected cells (n = 21) did not exhibit nonlinear membrane capacitance (Fig. 4(c)).

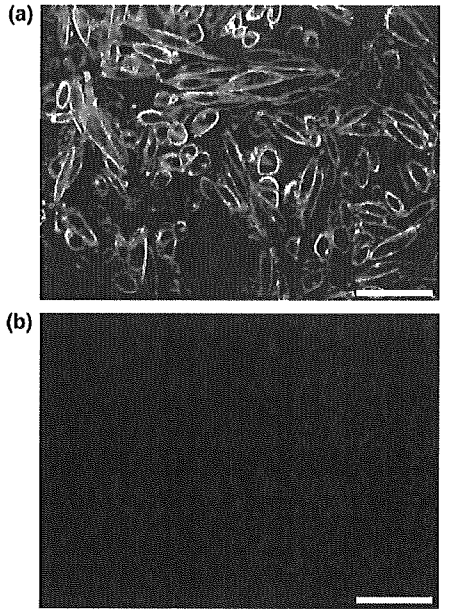

Fig. 2. Immunofluorescence images. (a) FLAG-tagged prestin-transfected CHO cell line. (b) Untransfected CHO cells. Fluorescent stains were observed in the transfected cell line after 4 months of subculture. By contrast, untransfected cells were not stained. Scale bars are 50 μm.

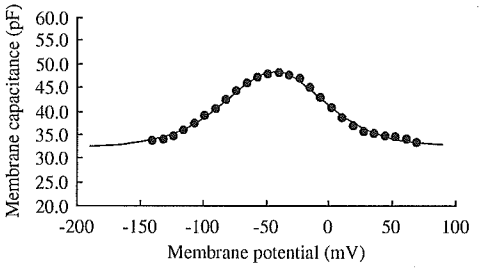

Fig. 3. Representative data of the voltage-dependent membrane capacitance of a guinea-pig OHC. Data points are fitted to Eq. (4), which is shown by the solid line. Fitting parameters are C_{lin} = 33.1 pF, Q_{max} = 2.33 pC, α = 28.0 mV and $V_{1/2}$ = −40.3 mV.

3.5. Efficient culture of FLAG-tagged prestin-expressing CHO cell line

When CHO cells which expressed FLAG-tagged prestin, the activity of which was confirmed by patch–clamp measurements, were cultured in CHO-S-SFM II medium, cells grew in suspension (Fig. 5). The electrophysiological properties of these cells were examined.

Table 1
Fitting parameters of the derivative of a Boltzmann function and charge density

	C_{lin} (pF)	Q_{max} (fC)	α (mV)	$V_{1/2}$ (mV)	Charge density (μm^{-2})
OHC (n = 11)	26.8 ± 3.7	2,878 ± 653	28.4 ± 2.3	−40.1 ± 9.5	6,830 ± 1,910
Wild-type prestin-expressing CHO cells (n = 20)	19.7 ± 4.1	75.5 ± 37.3	38.1 ± 4.8	−74.8 ± 11.6	246 ± 125
FLAG-tagged prestin-expressing CHO cells (n = 19)	24.5 ± 8.3	101.3 ± 51.9	38.0 ± 5.5	−73.0 ± 12.9	255 ± 88

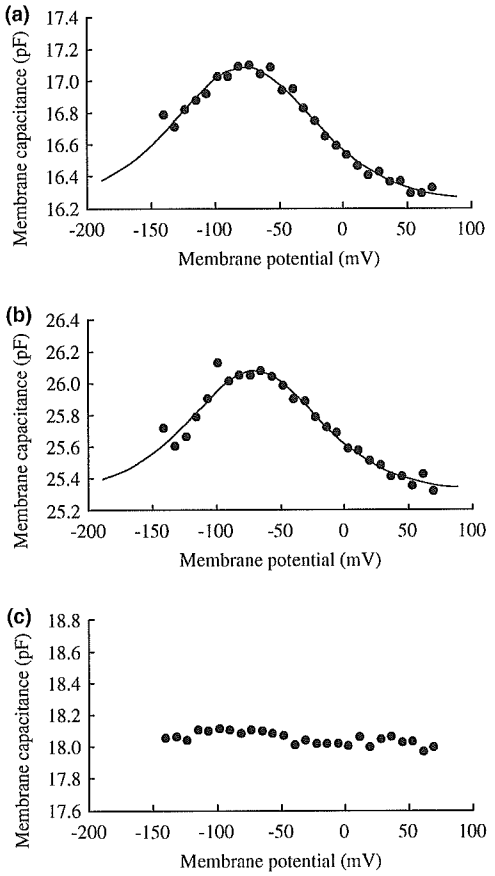

Fig. 4. Representative data of the measured membrane capacitance versus membrane potential. (a) Membrane capacitance of a wild-type prestin-expressing CHO cell. Data points are fitted to Eq. (4), which is shown by the solid line, with the following parameters: C_{lin} = 16.2 pF, Q_{max} = 127.1 fC, α = 36.8 mV and $V_{1/2}$ = −76.9 mV. (b) Membrane capacitance of a FLAG-tagged prestin-expressing CHO cell. Data points were fitted to Eq. (4), which is shown by the solid line, with the following parameters: C_{lin} = 25.3 pF, Q_{max} = 103.6 fC, α = 33.8 mV and $V_{1/2}$ = −70.4 mV. (c) Membrane capacitance of an untransfected CHO cell.

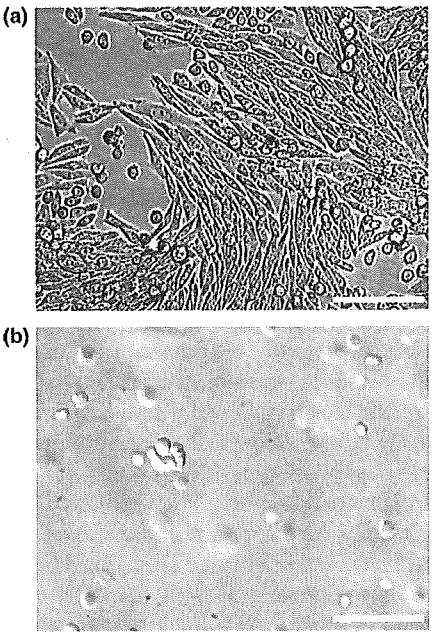

Fig. 5. Optical microscope images of FLAG-tagged prestin-expressing CHO cells. (a) Cells cultured in RPMI1640 medium containing 10% fetal bovine serum. (b) Cells cultured in CHO-S-SFM II medium. In (a), cells adhered to the culture dish and were spindle shaped. Spherical cells would be in the cell division phase. In (b), cells were suspended in the medium and were rounded. The focus plane was set above the bottom of the culture dish. Scale bars are 100 μm.

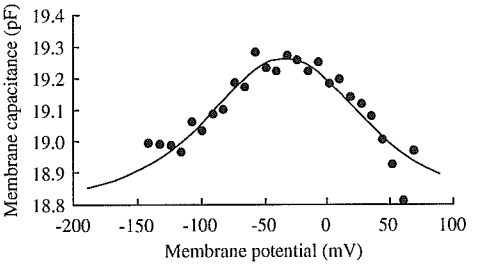

Fig. 6. Representative data of voltage dependent membrane capacitance of FLAG-tagged prestin-expressing CHO cells cultured in CHO-S-SFM II medium. Data points are fitted to Eq. (4), which is shown by the solid line. Fitting parameters are C_{lin} = 18.8 pF, Q_{max} = 70.7 fC, α = 39.8 mV and $V_{1/2}$ = −32.9 mV.

As shown in Fig. 6, when the measurements were performed at 36 h after passage, cells exhibited bell-shaped nonlinear membrane capacitance. This nonlinear membrane capacitance was fitted to Eq. (4), fitting parameters being C_{lin} = 18.8 pF, Q_{max} = 70.7 fC, α = 39.8 mV and $V_{1/2}$ = −32.9 mV. Nonlinear membrane capacitance similar to that shown by the data in Fig. 6 was observed at different points of time after passage.

Fig. 7 shows the time course of the cell density determined with a hemocytometer every 12 h (n = 4). It increased from 3×10^5 to 1×10^6 cells/ml and became saturated at 60 h after passage. The expression level of FLAG-tagged prestin every 12 h was assayed by Western blotting (Fig. 8). The bands around 90 kDa indicate prestin (Fig. 8(a)). The expression levels of prestin were evaluated based on the luminescence intensity of these bands, and the relative expression levels to the expression level in the cells cultured 12 h after passage were plotted against time (Fig. 8(b)). The expression level reached a maximum at 24 h after passage and then decreased.

4. Discussion

To obtain a large amount of prestin, we attempted to construct an expression system for prestin using *E. coli*, insect cells and CHO cells. Neither *E. coli* nor insect cells expressed prestin well. By contrast, prestin was found to